A hydroelasticity analysis of a damaged ship based on a two-way coupled CFD-DMB method

Yujia Wei [a], Atilla Incecik [a], Tahsin Tezdogan [b,*]

[a] *Department of Naval Architecture, Ocean and Marine Engineering, University of Strathclyde, 100 Montrose Street, Glasgow, G4 0LZ, UK*
[b] *Department of Civil, Maritime and Environmental Engineering, School of Engineering, University of Southampton, Boldrewood Innovation Campus, Building 176, Southampton, SO16 7QF, UK*

ABSTRACT

This study focuses on the numerical investigation of the hull girder loads on a flexible containership S175 with intact and damaged conditions advancing in regular head waves. In this study, a two-way coupled fluid-structure interactions framework is applied, in which the interactions between the flooding water inside the damaged tanks and wave fields are modelled by a Computational Fluid Dynamics toolbox OpenFOAM. The structural deformation is predicted using a multibody solver MBDyn. Hydroelasticity computations are performed for two different damage scenarios. The numerical results obtained show that the damaged ship experiences less vertical motions but greater global wave loads than the intact ship. It is also demonstrated that ship damages greatly influence the hull girder vertical bending moments (VBMs), while still water VBM is sensitive to the added weight from flooding water. In specific ship-damage conditions, local hogging moments at several amidship sections are found to exceed the limits specified by international regulations. Therefore, a new safety factor is recommended to avoid hogging moments of damaged ships remain below the limiting value. The results can also be used to determine whether the damaged ship will experience secondary damage due to hydroelastic response, helping with the design of future conventional ships.

1. Introduction

The safety of ships is the top priority for ship designers, ship owners and marine regulatory bodies. However, despite many efforts to improve the structural design of ships over the years, a serious damage to ship hulls continues to occur due to collision and grounding as well as to excessive loading. According to the statistical data from Lloyd's Register (Lloyd's_Register, 1996), a total of 76 ships were lost due to damage by collision, which occupied about 43% of the total loss, between 1991 and 1995. In recent years, two serious accidents occurred due to the failure of hull structure, MSC NAPOLI in 2007, and MOL COMFORT in 2013, as shown in Fig. 1. It was reported that both vessels were broken due to the large hogging of the hull structure.

The prediction of damaged survivability is challenging, since the damage openings at hull surface not only lead to flooding, but also reduce the local structural integrity. In such circumstances, ships may easily be excited by the inner and outer fluid loads. This forms a complex coupled system. The traditional rigid-body assumption may lead to the inaccurate prediction of hydrodynamic loadings as well as the resulting

ship motions. Therefore, a coupled Fluid-Structure-Interaction (FSI) method to predict the correct dynamic motion and hydroelastic responses of a containership in waves will have to be used for accurate load and response predictions.

The damage openings on a ship hull occur frequently during ship-to-ship collisions. Seawater floods into the damage compartment, which may result in sloshing which poses a serious risk to the ship's stability with a risk for capsize (Manderbacka et al., 2019). This mechanism may become more complicated when the ship sails in waves.

In order to investigate the phenomenon of flooding flow into a damaged compartment of a ship, a series of model experiments were performed accordingly. Ćatipović et al. (2018) obtained results from their model experiments and found that the wave-induced vertical motions (e.g., heave and pitch) of a damaged ship model were generally greater than that for an intact ship. In order to predict the stability of damaged ships, the nonlinear interaction between the water in the flooded compartment and ship motions has to be considered (Gao et al., 2013). Siddiqui et al. (2020) presented the results of a series of experimental studies of a 2D damage hull section in waves systemically

* Corresponding author.
  E-mail address: T.Tezdogan@soton.ac.uk (T. Tezdogan).

investigating the effects of wave parameters, damage compartment size and its opening sizes. Their results confirmed that for a floating damaged section in waves, the floodwater behaviour was highly coupled with body motions, and the overall behaviour was very different as compared to the intact condition.

Parallel with the experimental investigations, numerical simulations were developed to predict the dynamics of flooding water and damaged ship responses. Modified empirical Bernoulli equations were used to evaluate the flow rate through the opening. In addition, the lumped mass method (Manderbacka et al., 2015), shallow water theory (Santos and Guedes Soares, 2008) and MPS method (Hashimoto et al., 2017) were developed to predict the transient behaviour of damaged ship sections or ships associated with flooding. Subsequently, a fully nonlinear computational fluid dynamics method (Gao et al., 2013, Gao and Vassalos, 2015, Gao and Tian, 2021) was developed to improve the floodwater motions by considering the energy transaction between the water inside and outside the damaged compartment as well as the coupled effects between the damaged ship motions and fluid motions inside the damaged tanks.

Another important concern of a damaged ship is the reduction of its structural strength due to the loss of load-carrying structural elements. In such circumstances, the damaged ship may be more vulnerable to lose its structural integrity due to the environmental loads. The seawater dynamics in a damaged compartment significantly changes the load distribution on a ship hull in longitudinal direction, which greatly affects not only the still-water bending moment (S_VBMs), but also the wave-induced bending moment (W_VBMs) (Lee et al., 2012; Mikulić et al., 2018).

There has been a great deal of research devoted to investigate the influences of damaged ships on the W_VBMs. For example, Chan et al. (2003) proposed a nonlinear time-domain simulation to predict the dynamic structural loads on a Ro-Ro ship in regular waves in intact and damaged conditions. The authors obtained higher global wave loads and VBMs for a damaged ship than those evaluated for intact conditions. Fols⊘ et al. (2008) and Lee et al. (2012) presented different linear methods for numerical simulations on a damaged oil tanker and warship. Their results confirmed that the magnitudes of W_VBM for damaged ship conditions were about 11%–15% greater than intact ship in heading seas. Begovic et al. (2017) conducted experimental investigations of hull girder loads on an intact and damaged naval ship DTMB5415 at zero speed in both head and beam regular waves. The researchers reported that the vertical shear force (VSF) and VBM values are significantly larger for the damaged ship in heading waves, with an approximate 10% increase compared to the intact ship in the whole wave range tested. Similar experimental studies were conducted by Ćatipović et al. (2018), reporting a 28% increase in W_VBMs of the damaged ship compared to the intact ship. Mikulić et al. (2018) proposed an efficient method to evaluate the vertical bending moment of a damaged ship in different wave directions through an in-house MATLAB code, and the hydrodynamic forces were calculated using WAMIT. The authors concluded that the wave-induced VBM of the damaged ship was generally larger than that of the intact ship, especially for stern-quartering waves.

Based on the above statements, even if the ship has survived the damage from the perspective of stability, it can still suffer from the risk of increased longitudinal W_VBM of the hull girder (Begovic et al., 2013). The enlarged vertical loads on the hull girder may further lead to secondary damages, i.e., deformations or even collapses. Under these circumstances, it is important to estimate the correct W_VBMs of a damaged ship with the considerations of the ship hull elasticity and flooding water dynamics as suggested by the Soares et al. (2009).

Therefore, a novel FSI model was established in this study, which filled in the gap that the majority of the numerical models on the damaged ship studies in the open literature assumed the ship as a rigid body, in which the hydroelastic loads on the hull girder for a damaged ship were not considered. In this study's proposed FSI framework, a two-way CFD-DMB method was applied, where the intake flooding water pressure and hydrodynamic loads exported from the CFD calculations were used to derive the structural responses in the DMB solver, and the structural deformations were fed back into the CFD solver to deform the mesh. To communicate data between the CFD and multibody solver, a two-way coupling algorithm was implemented to transfer the fluid loads and structural deformations effectively. Our previous studies (Wei et al., 2022; Wei et al., 2022) evaluated the performance and accuracy of the coupling solvers on an elastic-demonstrated containership in regular and focused wave conditions. This paper extends our previous studies (Wei and Tezdogan, 2022a,b) by investigating the seakeeping and hydroelastic behaviour of the S175 containership in both intact and damaged conditions with considerations of the dynamics of flooding water, motion effects and the elastic ship deformations.

The number of damaged compartments and their positions were studied based on the proposed FSI model to investigate their effect on flexible ship seakeeping and hydroelastic behaviour. This will help to gain more insight into our understanding of the dynamic damaged ship behaviour in waves, including the interactions between the flexible ship and flooding water, the violent free surface phenomena (e.g., sloshing) and longitudinal structural load distributions. This study will be valuable in better assessing the damaged ship behaviours and the wave-induced global and local loads with the consideration of ship hydroelasticity, which assists in rapid decision-making relevant to post-damaged evacuation and maintenance. The results of this paper will also shed some light on improving the current legislation on the safety of ships in damaged condition by the international SOLAS (Safety of Life at Sea) convention.

The rest of this paper is organised as follows: in Section 2, the numerical methodologies used in the present study are discussed. In Section 3, the detailed problem statements and model testing set-up are discussed. In Section 4, the verification and validation studies are presented. In Section 5, the numerical results of the study on the dynamic motions of the flexible ship in intact and two damaged scenarios are illustrated. A series of numerical results, including dynamic flooding water, flexible ship motions and structural loads are also analysed. Virtual observations of the free surface elevations inside the damaged tank are shown accordingly. The conclusions and future recommendations are drawn in the final section.

Fig. 1. Two major accidents in recent years (Sun et al., 2021): (a) MSC NAPOLI, (b) MOL COMFORT.

2. Numerical model

This study demonstrated a fully coupled fluid-structure-interaction (FSI) model based on a partitioned approach to separate the complex physicals into the fluid and structure parts and solve them iteratively. The open-source CFD toolbox OpenFOAM was applied to model the fluid field by solving the nonlinear Reynolds-Averaged Navier Stokes (RANS) equations using a Finite Volume Method (FVM). The structure solver "MBDyn" was adopted to calculate the structural displacements and deformations by solving the Lagrange equations. An in-house data coupling library was implemented to transfer the data through the fluid and structure solvers based on a two-way algorithm. The main features of the fluid, solid solver and the coupling approach are presented in the following sub-section.

2.1. Fluid solver

The simulation of fluid flow was performed based on an open-source CFD toolbox OpenFOAM using the multi-phase solver interFoam. In this model, the flow was assumed to be incompressible and viscous, which was governed by the continuity and momentum equations as given below:

$$\nabla \cdot U = 0 \tag{1}$$

$$\frac{\partial \rho U}{\partial t} + \nabla \cdot \left(\rho \left(U - U_g \right) \right) = - \nabla P_d - g \bullet x \nabla \rho + \nabla \left(\mu_{eff} \nabla U \right) + (\nabla U) \bullet \mu_{eff} + f_\sigma \tag{2}$$

where U refers to the velocity of flow field, ρ is the mixed density of water and air, g is the gravity acceleration, P_d refers to the dynamic pressure, μ_{eff} is the effective dynamic viscosity, f_σ is the surface tension which is only considered at the free surface.

The Volume of Fluid (VOF) method (Hirt and Nichols, 1981) was adopted to simulate the free surface in the numerical domain by solving an additional transport equation for the scalar quantity, a, which represents the volume fraction of fluid for each cells.

$$\frac{\partial a}{\partial t} + \nabla \bullet \left[\left(U - U_g \right) \right] a + \nabla \bullet \left[U_r (1 - a) a \right] = 0 \tag{3}$$

where U_r is the artificial compressive velocity which only functions near the free surface due to the inclusion of $(1 - a)a$.

For a two-phase flow problem, the volume fraction of each phase was used as the weighting factor to calculate the mixture properties. The equations for the density and the viscosity can be expressed by:

$$\rho = a\rho_w + (1 - a)\rho_a \tag{4}$$

$$\mu = a\mu_w + (1 - a)\mu_a \tag{5}$$

where subscripts w and a represent the water and air phases, respectively.

An open-source toolbox "waves2Foam" (Jacobsen et al., 2012) was applied in this study to generate and absorb free surface waves in the numerical wave tank (NWT). The relaxation zone technique was adopted to provide better wave quality near the inlet boundary and remove spurious reflection at the outlet boundary. The following equations specify the primary function of the relaxation zones:

$$a_R(\chi_R) = 1 - \frac{\exp(\chi_R^{3.5}) - 1}{\exp(1) - 1} \tag{6}$$

$$\varphi_R = \omega_R \varphi_R^{computed} + (1 - \omega_R) \varphi_R^{target} \tag{7}$$

where φ_R refers to either the velocity or volume fraction of water a. The weighting function a_R is always equal to 1 at the interface between the non-relaxed computational domain and the relaxation zones, χ_R is a

value between 0 and 1. The relations between χ_R and a_R are shown in Fig. 2. A series of surface elevation gauges (WP1–WP3) were placed inside the wave domain: WP1 and WP3 were placed inside and close to the regions of wave generation and wave absorption to control the wave quality. WP2 was located inside the wave propagation region (1.5m in the front of ship bow) to monitor the free surface elevations interact with the hull.

The incident waves were generated based on the second-order Stokes Wave Theory, with the resulting expression of free surface and velocity components are:

$$\eta = \frac{H}{2} \cos(\theta) + k \frac{H^2}{4} \frac{3 - \sigma^2}{4\sigma^3} \cos(2\theta) \tag{8}$$

$$u = \frac{H}{2} \omega \frac{\cosh(kz)}{\sinh(kz)} \cos(\theta) + \frac{3}{4} \frac{H^2 \omega k \cosh(2kz)}{4 \sinh^4(kh)} \cos(2\theta) \tag{9}$$

$$w = \frac{H}{2} \omega \frac{\sinh(kz)}{\sinh(kz)} \sin(\theta) + \frac{3}{4} \frac{H^2 \omega k \sinh(2kz)}{4 \sinh^4(kh)} \sin(2\theta) \tag{10}$$

where H is the wave height, wave propagation angle $\theta = kx - \omega t + \psi$ with k is the wave number, ω is the angular wave frequency and ψ is the wave phase and $\sigma = \tanh(kh)$.

2.2. Multibody solver

The structure solver applied in this study is MBDyn, which adopts a Lagrange multiplier or redundant coordinate set formations for a multibody system. Compared to the reduced coordinate set method, where only minimum numbers of degrees of freedom (DoFs) are used to describe the motion of the system, a redundant formulation which allows 6 DoFs motion for each body and constraints is enforced by Lagrange multiplier (Masarati et al., 2014).

For each body of the system, Newton-Euler equations of motion were established in the differential-algebraic form as a set of first-order equations together with the constraint equations, resulting in a system of Differential-Algebraic Equations (DAE) as follows.

$$M\dot{x} = P \tag{11}$$

$$\dot{P} + \varphi_x^T \lambda = f(x, \dot{x}, t) \tag{12}$$

$$\varphi(x, t) = 0 \tag{13}$$

where M denotes the inertia matrix of the rigid body, x denotes the translational and rotational parameters in the global reference frame. P refers to the momentum of the body. λ denotes the vector of the Lagrange multipliers for the constraints; f is the external force and moment vector exerted upon the body which might be related to its displacement and velocity as well as time. φ is a set of kinematic constraints applied on the body and φ_x^T is the Jacobian of φ with respect to the generalized coordinate.

The distance between each two adjacent nodes was taken as a Euler-Bernoulli beam to consider the effects of structural deformations, as shown in Fig. 3. The beam element used in the present study is a three-node beam element which was implemented in the MBDyn software by a finite volume approach for the multibody formulation of three-node beam elements based on the Geometrically Exact Beam Theory (GEBT) (Ghiringhelli et al., 2000). The internal forces and moments were evaluated at the evaluation points (shown in Fig. 3) and the geometrical strains and curvatures via the constitutive law are calculated based on the following equations.
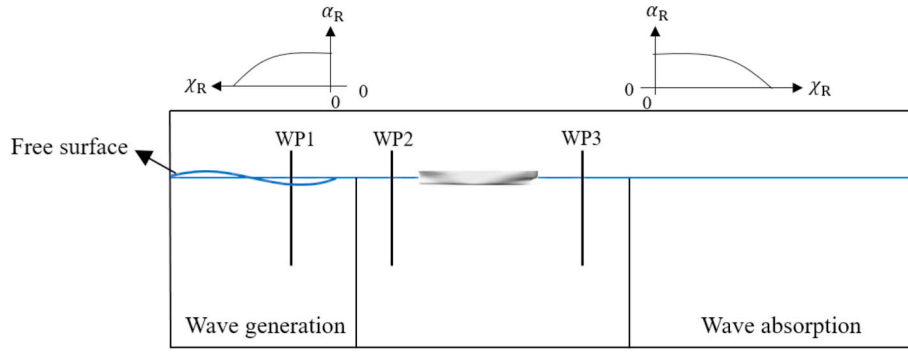
Fig. 2. Diagram of the variation of χ_R and a_R in relaxation zones and probes positions.
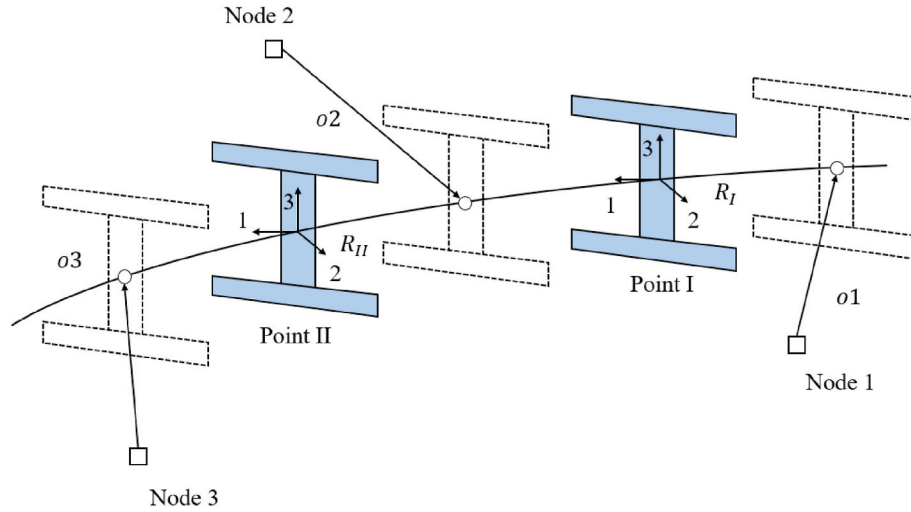

Fig. 3. An example of a three-node beam element geometry (Ghiringhelli et al., 2000).

$$\begin{Bmatrix} F_x \\ F_y \\ F_z \\ M_x \\ M_y \\ M_z \end{Bmatrix} = f \left\{ \begin{Bmatrix} \varepsilon_x \\ \gamma_y \\ \gamma_z \\ \kappa_x \\ \kappa_y \\ \kappa_z \end{Bmatrix}, \begin{Bmatrix} \dot{\varepsilon}_x \\ \dot{\gamma}_y \\ \dot{\gamma}_z \\ \dot{\kappa}_x \\ \dot{\kappa}_y \\ \dot{\kappa}_z \end{Bmatrix} \right\} \tag{14}$$

where F_x is the axial force component, F_y and F_z are the shear force components, M_x is the torsional moment component, M_y and M_z denote as bending moment components; ε_x, γ_y and γ_z are axial strain and shear strain coefficients, κ_x, κ_y and κ_z are the bending curvature parameters, and f is an arbitrary function of beam material constitutive law.

2.3. FSI data coupling procedure

After computing the dynamic responses in the structure solver, the structural displacements and rotations should be transferred back to the CFD solver. A two-way FSI algorithm was applied between OpenFOAM and MBDyn solvers in an iteratively staggered coupling regime. Two solvers communicate through sockets; OpenFOAM solver worked as the main solver, and MBDyn reacted as the slave solver. The communication data were transferred within each sub-cycling, until the PIMPLE algorithm converged, so as to stabilize the simulation and preserve equilibrium conditions on the interface. It is worth noting that the PIMPLE Algorithm is a combination of PISO (Pressure Implicit with Splitting of Operator) and SIMPLE (Semi-Implicit Method for Pressure-Linked Equations).

The workflow of the present CFD-DMB approach is shown in Fig. 4, and for detailed descriptions a reference can be made to our previous paper (Wei et al., 2022). To give a brief summary, inside the data communication scheme, the scalar quantities of pressure and wall shear stress of each ship section were calculated from the CFD solver and mapped onto the structure nodes in MBDyn. By accepting the force data, the MBDyn predicted the structural responses and then feed the updated position data back to the CFD solver. The fluid mesh has to be updated simultaneously based on the dynamic mesh technique of mesh motion, which relies on the solution of Laplace transport equations for the displacement point fields.

3. Problem statement

3.1. Intact and damaged ship

In this study, the standard S175 containership with a scale ratio of 1:40 was used as a case study in intact and damaged conditions. The ship model did not have any appendages. The longitudinal body shape of the intact ship model is shown in Fig. 5.

Since ship damage may occur in many ways, in this study we only focused on the side damage type of hull openings where the ship may experience collision with ice or other marine structures. The damaged parameters (e.g., damaged tank numbers and locations) were generally random quantities that may be described by the probability distribution. Such probability distributions in the cases of collision damages were regulated by the International Maritime Organization (IMO, 2003). The numerical model developed by Parunov et al. (2015) defined credible damaged scenarios based on Monte Carlo (MC) simulation according to IMO probabilistic models. In his model, a set of 1000 random samples
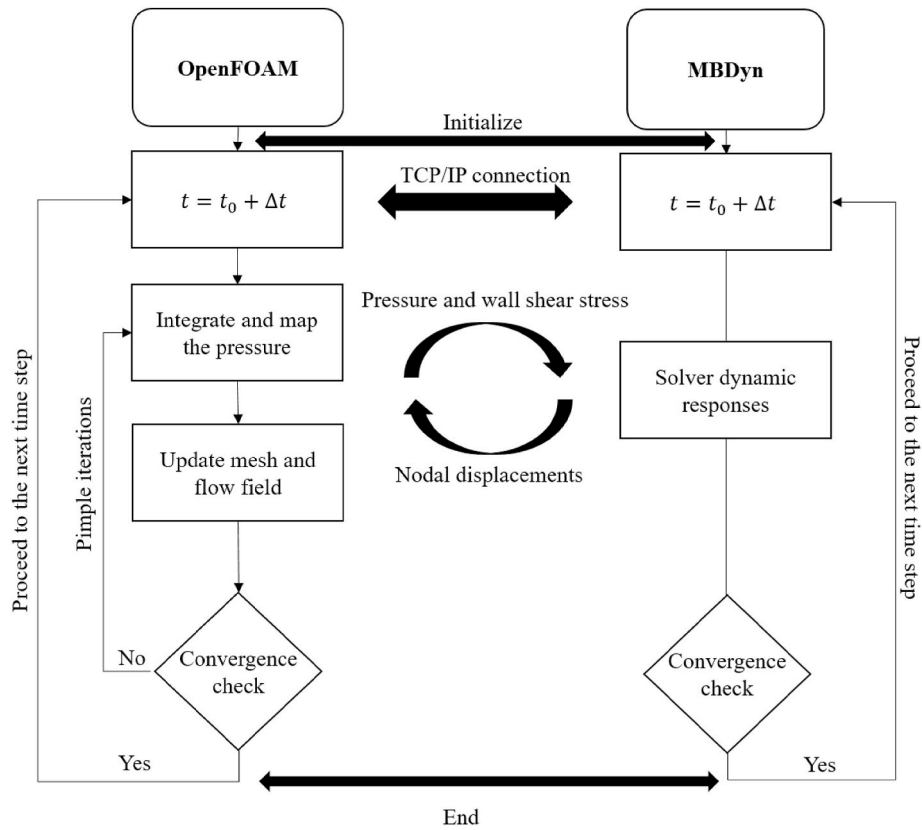
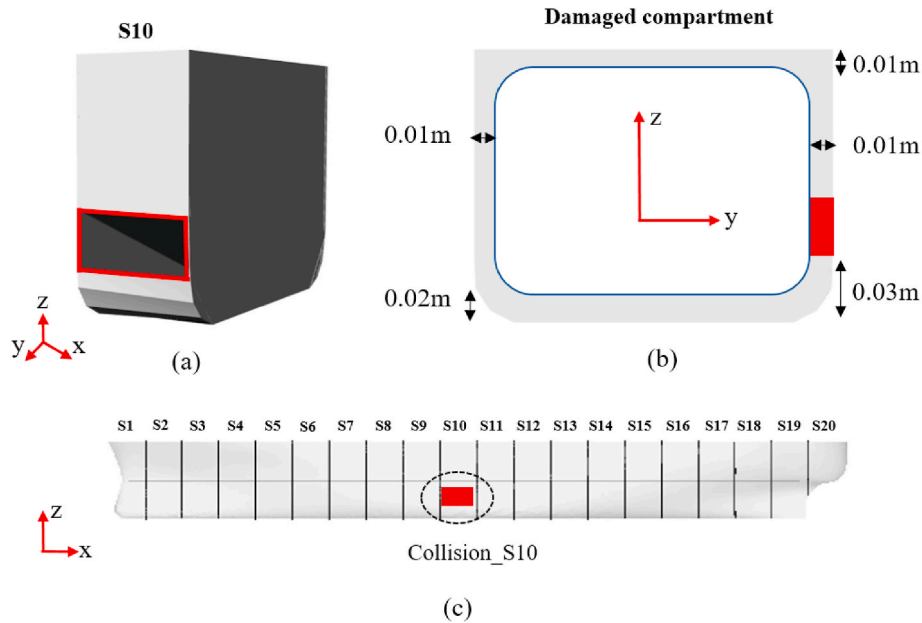**Fig. 4.** The workflow of two-way CFD-DMB coupling framework.

Fig. 5. Damaged tank specifications.

were drawn according to the IMO recorded accidental models. The results showed that in the cases of collision damage, the probability of single-tank damage or double-tank damage are the highest, followed by three tanks damage which comes second. Based on these considerations, plausible damage scenarios were defined for the purpose of the present study. For the damage of collision case studies, damaged tanks at the ship starboard were assumed in this study, resulting in asymmetrical

damage, as shown in Fig. 5(a and b). The damage at the amidship (ship section 10) was shown as a representative image in Fig. 5(c) where the damaged opening in this scenario has a uniform rectangular shape of 0.22m × 0.11m on the starboard side, accounting for 5% of the total ship's length and 22% of the ship depth. Each damaged compartment had a ventilation hole to minimise the effects of spurious entrapment of air between the intake water and inner hull. The main particulars of the

intact and damaged ship models are summarised in Table 1.

The positions of all pressure gauges are depicted in Fig. 6. An array of 4 pressure gauges (P0–P3) were placed on the bow flare and bow bottom areas of the ship to investigate the wave-induced impact pressure of the ship during the water enter of bow.

3.2. Structural model development

A discrete module beam model (DMB) in conjunction with a multi-segment partitioning technique was employed in MBDyn to formulate the structural models of the selected ship model, as shown in Fig. 7. The development of such a beam model for the intact S175 containership was explained in the authors' previous paper (Wei et al., 2022). In its numerical representation, the hull surface was divided into 20 sections, each section was served as a structural node and attached with a body element, as shown in Fig. 7. It is seen that a series of 19 beam elements, equivalently representing the structure's stiffness, were employed to connect the neighbouring body elements. It is worth noting that the beam was restraint to have torsional and horizontal bending effects, therefore the total-joint type (TJ) of elements were applied. A number of 39 total joints were used to connect the beginning node N1 with the every another node (N2–N20, N1′-N19′), imposing constraints, where the free-free beam was permitted only deformed in vertical direction. Another set of total joint element (CJ1) was applied between midship node (N11) and the background node (N0) to suspend the surge motion of ship beam from the drift force. As a result, the DMB ship beam design in this study was allowed to have heave and pitch motions and experience the vertical bending effects. The detailed configuration of the DMB beam model was summarised in Table 2.

As mentioned above, the DMB method provides an efficient method to define the local structure characteristics of the ship by using the equivalent beam element stiffness. To check the hull girder residual strength for damaged ships, it is important to determine the damage forms and the main parameters to characterise the damaged degree. In this study, the stiffness loss of the side-damaged containership was assessed using Zhang et al. (2021)'s method based on the calculation of the loss of section modulus and the stiffness loss of the structure. This method reduces enormous modelling efforts and computing time against other methods, e.g., the simplified progressive collapse method (Smith, 1977) and nonlinear finite element analysis (FEA). The authors validated model's applicability on 13 types of ship damage scenarios with favourable agreement compared to the results of FEM. In their approach, the stiffness loss of the hull girder with side opening type of damages (symmetric about the neutral axis) was approximately 1.28%–1.69% of total beam stiffness. It is worth highlighting that if the ship's double

bottom loses its capacity to withstand the longitudinal stress, the hull girder residual strength will reduce significantly, i.e., 14.8%–38.3% of the overall stiffness based on the predictions from Zhang et al. (2021). Therefore, in this study the residual strength of the hull girder was accounted by applying a 2% structure loss on the local stiffness of beam elements at the damaged tank position.

3.3. Modal analysis (intact ship)

The vibration behaviour of the DMB ship-beam model for an intact containership was earlier examined by Wei et al. (2022). To give a brief summary, the eigenvalues f_b of the free-free beam up to the fourth order were estimated in dry condition using the Arpack solver in MBDyn as listed in Table 3. Although MBDyn does not support the wet modes analysis, the wet-mode eigenvalues of the ship-beam model have previously been investigated using a commercial FEA software Abaqus (Wei et al., 2022). It is seen from Table 3 that the dry-mode beam eigenvalues were shown favourable agreement with the experimental results f_s by Jiao et al. (2021a,b,c). The beam cross-section profiles, including the height and width, were modulated by matching the natural frequencies with the real ship vibration (mainly 2nd mode). The closed beam profile with a rectangular cross-section of 0.08m × 0.05m was selected and applied in this study's later cases.

It is worth pointing out that the predictions on the eigenvalues of the damaged ships pose difficulties since the load distributions of a damaged ship change in time and space due to the fluctuation of the dynamic flooding water. One possible method is to calculate the damaged ship eigenvalues in a steady state, i.e., the damaged ship floats in still water, therefore, the mass of flooding water is treated as a static lump mass.

3.4. CFD configuration

3.4.1. Computational domain

The computational domain was established in the CFD computations to simulate ship sailing in head waves. The domain was extended in three dimensions, i.e., $-1.75L < x < 2.5L$, $-1.2L < y < 1.2L$ and $-1.5L < z < 0.5L$, where L refers to the ship length between perpendiculars. A general view of the wave domain (for the ratio of the wavelength to the ship length of $\lambda/L = 1.2$) is shown in Fig. 8. The three-dimensional ship model was applied, but only the centre line plane of the ship was shown in the figure. It can be seen that the aside boundaries were placed far away from the shipboard sides to reduce the influence of wave reflection from numerical boundaries. Inside the numerical domain, the global Cartesian coordinate system was set at the same height level with the calm water surface, coinciding with the aft-perpendicular and the ship's centreline. The global reference frame with the positive directions of the x, y, z pointed to the ship stern, port side and the domain atmosphere, respectively. Damage was modelled in a way that damaged tanks are flooded up to the still water level corresponding to the ship's initial draft, in case of significant transient responses caused by the sudden influx of flooding water.

The boundary conditions applied to the numerical wave tank are summarised in Table 4. At the inlet boundary, the wave velocity was prescribed for the superposition of wave and current speeds, while the pressure was set as fixed flux pressure that adjusts the pressure gradient. At the outlet boundary, the inlet-outlet boundary provided a zero-gradient outflow condition to remain the flux inside the domain. The domain bottom was set as type of wall to model deep-water seabed.

where WV is wave velocity, OPMV denotes as outlet phase mean velocity, PIOV represents pressure inlet outlet velocity, MWV is moving wall velocity, FFP is fixed flux pressure, ZG is zero gradient, TP is total pressure, IO is inlet outlet. kqRWF, nutkRWF and omegaWF are turbulence wall functions.

3.4.2. Mesh and solver settings

The finite volume mesh was generated using the OpenFOAM mesh

Table 1
Principal particulars of the intact and damaged S175 containership.

| Main particular	symbol	Full scale	Model
Scale	C	1:1	1:40
Length between perpendiculars	L(m)	175	4.375
Breath	B(m)	25.4	0.635
Depth	D(m)	19.5	0.488
Draft	T(m)	9.5	0.238
Displacement	Δ (kg)	23,711	370
Block coefficient (C_b)	C_b	0.562	0.562
Longitudinal center of gravity (LCG) from aft perpendicular (AP)	x_g (m)	84.98	2.125
Vertical center of gravity (KG) from base line	z_g (m)	8.5	0.213
Transverse radius of gyration	k_{xx} (m)	9.652	0.241
Longitudinal radius of gyrations	k_{yy} (m)	42.073	1.052
Damage opening area	S_d (m²)	0.952	0.0238
Damage opening length	L_{Dl} (m)	8.8	0.22
Damage opening height	L_{Dh} (m)	4.32	0.108
Damage opening compartment (S10) from FP	L_{S10} (m)	81.8	2.045
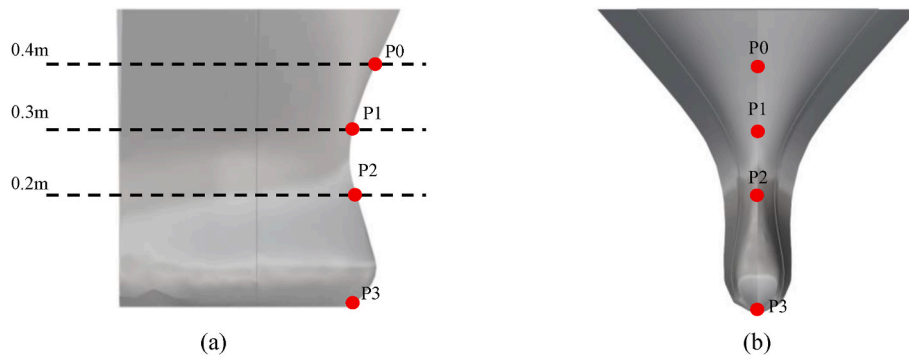
Fig. 6. An overview of the pressure gauge placements on the ship bow section (a) ship starboard, (b) ship front view.
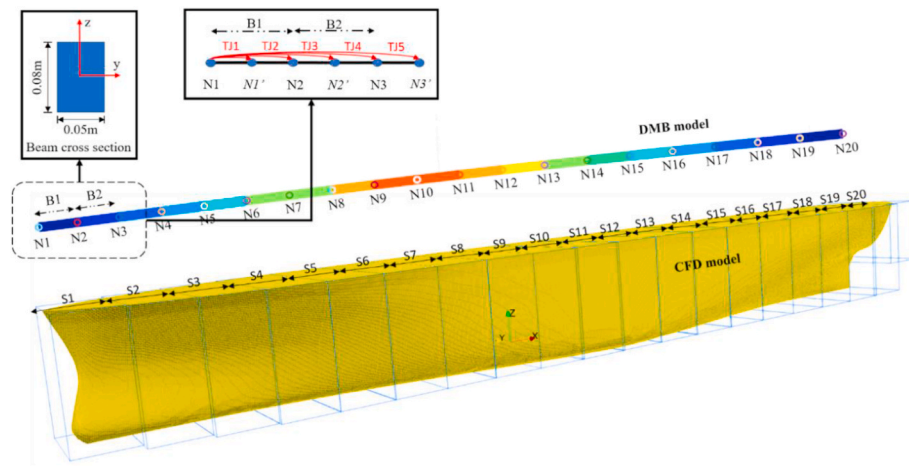

Fig. 7. DMB ship-beam model demonstration in MBDyn.

Table 2
Detailed demonstration of DMB beam model.

MBDyn settings	Functions	Number
Structural nodes	Background node (N0)	1
	Beam node (N1–N20, N1′-N19′)	39
Body elements	(Body1-Body20)	20
Beam elements	(B1–B19)	19
Joint elements	Clamp joint elements (CJ1)	1
	Total joint elements (TJ1-TJ39)	39

Table 3
Calibrated beam natural frequency properties and error (f_b denotes MBD beam dry-mode natural frequency and f_s is the ship natural frequency from experiment) (Jiao et al., 2021).

Order	Mode	f_b (Hz)	f_s (Hz)	Error (%)
1st	2	10.140	10.154	0.112%
2nd	3	26.116	26.241	0.482%
3rd	4	49.136	49.747	1.246%

generation utility, snappyHexMesh based on the cell splitting and mesh fitting techniques (Jasak et al., 2007). The background mesh was generated using the uniform hexahedra cells and extracted automatically according to the surface geometries in Stereolithography (STL) format. Then, the surface meshes were snapped to the geometry by iteratively refining the background mesh and deforming the resulting split hexahedra cells to the surface. The mesh refinements can flexibly be specified on edges, surfaces and volumes to preserve the optimum geometry feature resolutions. The grids density at the free surface for multi-phase studies was required to be refined in order to maintain the VOF phases sharp. A minimum of 110 cells per wavelength and 12 cells per wave height were used on the free surface modelling, which fulfilled the guideline from ITTC (2017). To ensure that the high Reynolds number flow features were approximately captured, the grid density at the region close to the ship hull was further refined several times using volumetric controls, primarily maintaining the adjacent wall layer-thickness $y+$ value below 30. A detailed surface mesh at the geometry is shown in Fig. 9.

To solve the pressure velocity coupling equations, PIMPLE was utilised. The two equations $k-\omega$ SST model was selected in the present study, which blended the advantages of the near-wall accuracy of the $k-\omega$ model and the free-stream accuracy of the $k-\varepsilon$ model. To mimic the significant decrease in wave height due to the turbulence effects, the stable $k-\omega$ model developed by Devolder et al. (2018) was implemented in this study,

4. Verification and validations

4.1. Sloshing tanks

The first validation case was presented for a 2D sloshing problem in order to test the performance of the CFD solver in solving nonlinear free surface flow and capturing the sloshing effects. In this validation study, a two-dimensional moving tank extends into two directions, i.e., $0 < x < 0.57$ m, $0 < z < 0.3$ m. Three free surface probes (P1–P3) were placed in the middle and two sides of the domain, as shown in Fig. 10. Two-turbulence models, $k-\omega$ SST and $k-\varepsilon$ were tested with the turbulence wall functions applied at wall tanks. The tank is moving periodically with a speed amplitude of $a = 0.005$m and shaking frequency
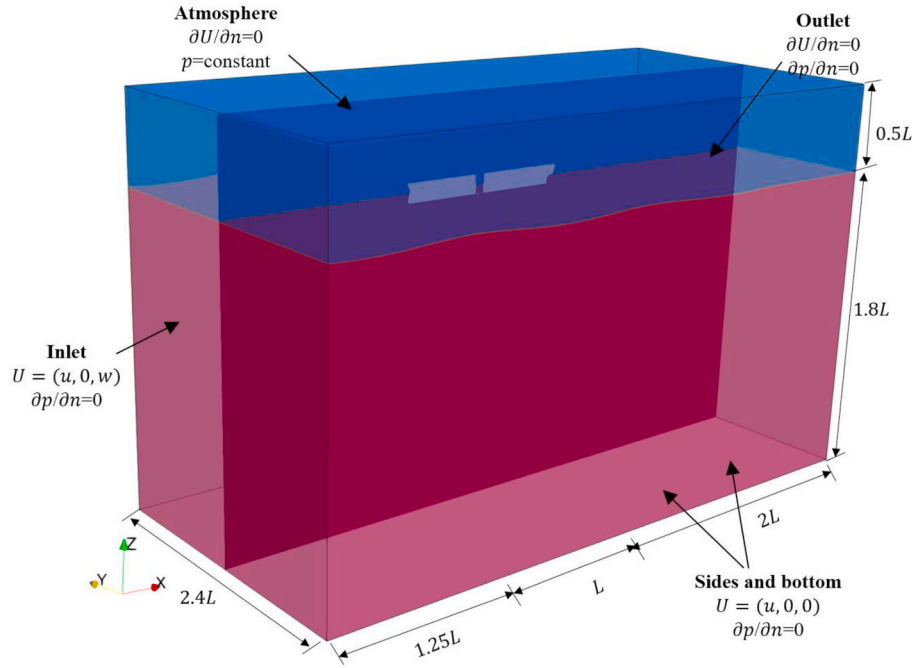
Fig. 8. Computational domain and boundary conditions.

Table 4
Summary of the boundary conditions in OpenFOAM.

	Inlet	Outlet	Atmosphere	Hull
U	WV	OPMV	PIOV	MWV
P_rgh	FFP	ZG	TP	FFP
Alpha.water	FV	VHFR	IO	ZG
K (k)	FV	IO	IO	kqRWF
Nut (ν_t)	FV	ZG	ZG	nutkRWF
Omega (ω)	FV	IO	IO	omegaWF

$w_0 = 6.0578 \text{ s}^{-1}$, which is consistent with the experimental settings of (Liu and Lin, 2008). The time step size was selected to be 0.005s. The numerical model runs up to 20s with 40 cores and consume about 0.3 CPU hours. The numerical results of free surface displacement (η) obtained in all three wave probes are shown in Fig. 11 and further compared to the experimental data of Liu and Lin (2008) with a reasonably well agreement. It can be concluded that the selected multi-phase solver is successful in solving the complex physics inside the sloshing tank and it is applicable for further damaged ship seakeeping

analyses.

4.2. Free surface waves

Wave modelling is of prime importance for the wave-structure interaction problems. In this study, the presence of ship forward speed was modelled by implementing an additional uniform current at the boundary inlet and coupled with the waves based on the combined wave-current function. The encounter wave frequency was used to generate the desired the wave group. A series of regular head waves were generated ranging from ($\lambda/L = 0.9$–1.6), with a constant wave height ($H = 0.12$m) and uniform flow speed ($U = 1.80$ m/s). The wave shapes monitored at the wave probe WP2 were plotted in Fig. 12. As can be seen from the figure, the CFD simulated waves (λ/L_N) are in very good agreement with the theoretical values (λ/L_T) among all wave frequencies. The decay in wave amplitude is less than 7% over time for most wave conditions. It can be concluded that the CFD method can provide reliable wave generations for the subsequent predictions of ship motion responses. The averaged wave amplitudes over the last five stable wave periods were used to further calculate the motion response
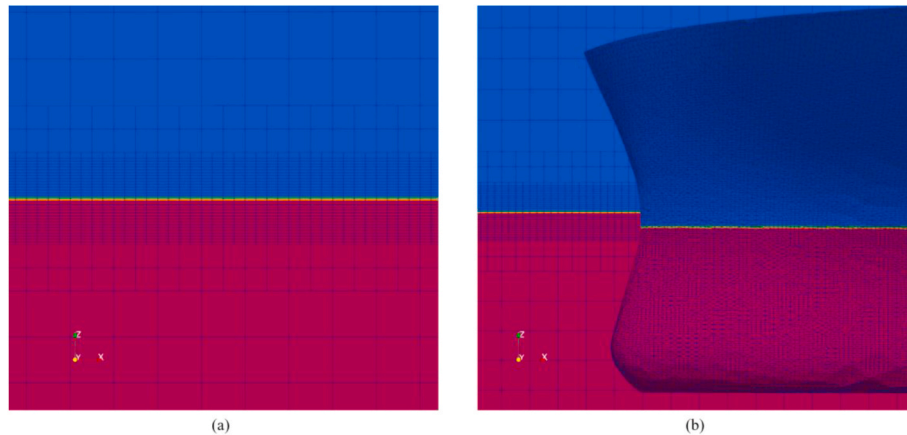

Fig. 9. Mesh refinement zone and boundary layer close the structure hull.
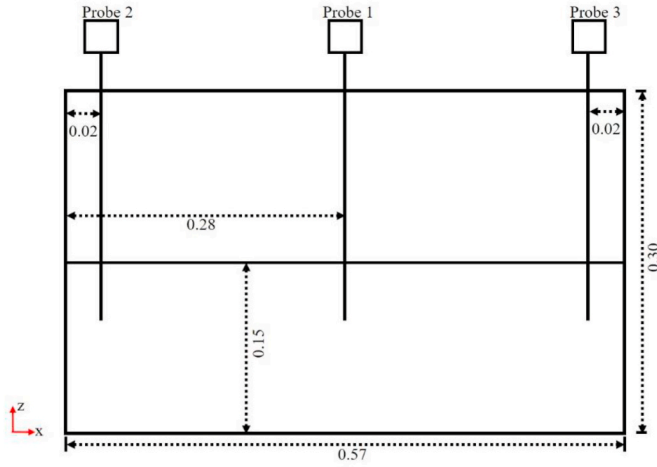
Fig. 10. The two-dimensional (2D) sloshing tank layout.

amplitude operators (RAOs) in the following sub-sections.

4.3. Flexible ship in waves

The uncertainty study caused by the modelling and simulation of fluid dynamics by a CFD solver are generally much greater than the uncertainties associated with the structural responses by a FEA solver (Huang et al., 2022). Therefore, a verification study was undertaken on the CFD solver following the Grid Convergence Index (GCI) method (Stern et al., 2006) to assess the simulation numerical uncertainty of the flexible ship with intact condition in waves. The numerical simulation error and uncertainty U_{SN} mainly includes the accumulation from iterative error U_I, grid size error U_G and time step error U_T. It is known that the uncertainty in iteration error U_I is negligible compared with the grid size and time step (Tezdogan et al., 2015). Therefore, only the grid and time step sensitivity studies were carried out following the GCI uncertainty procedure in the present verification study.

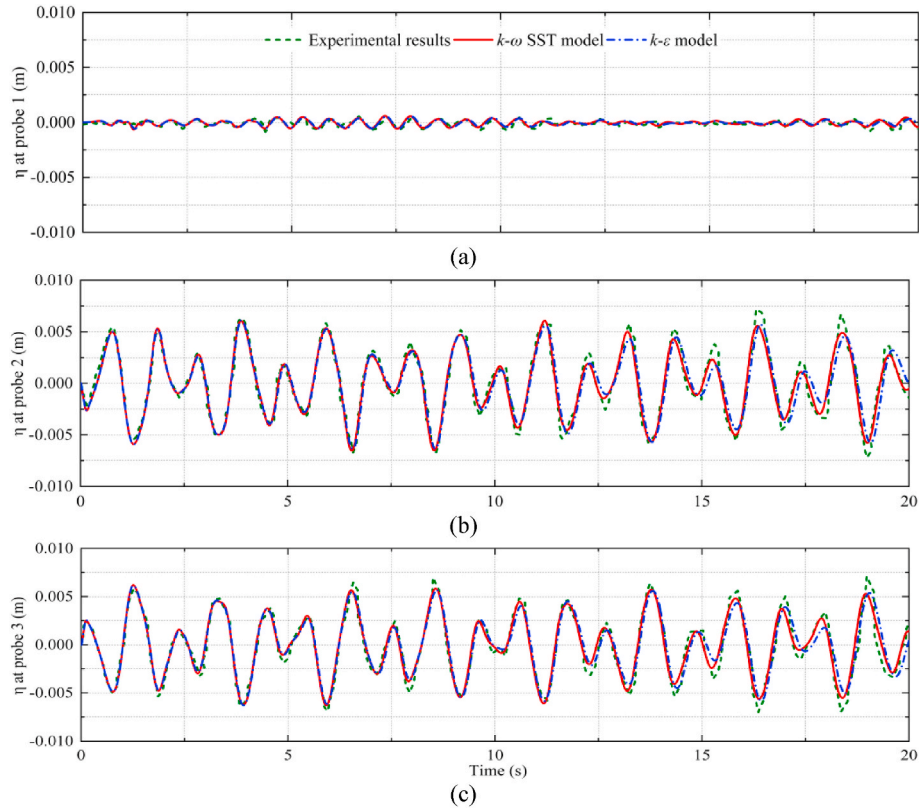$$U_{SN}^2 = U_I^2 + U_G^2 + U_T^2 \tag{15}$$

Fig. 11. The numerical results extracted from wave probes compared to the experimental results and analytical results: (a) Wave elevation monitored at probe 1, (b) Wave elevation monitored at probe 2, (c) Wave elevation monitored at probe 3.
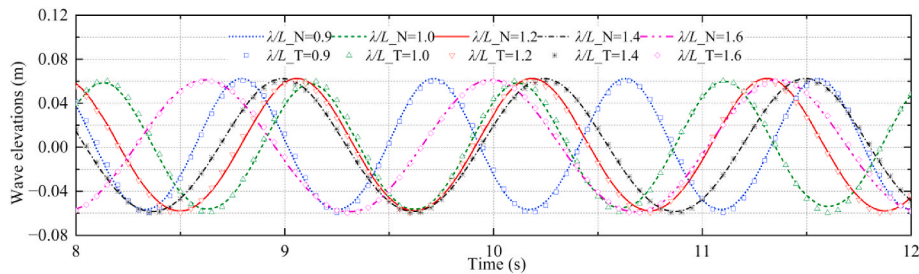

Fig. 12. Time-series wave elevation monitored at WP2 and compared to the theoretical wave shapes.

Grid and time convergence studies are performed by means of three solutions which are refined systematically with refinement ratio. Define S_{k1}, S_{k2} and S_{k3} to be the solutions with fine, medium and coarse input parameters. The subscript k refers to the kth input parameters (i.e., G for grid size and T for time step). Differences between medium-fine $\varepsilon_{k21} = S_{k1} - S_{k2}$, and coarse-medium $\varepsilon_{k32} = S_{k3}-S_{k2}$ solutions are used to define the convergence ratio:

$$R_k = \frac{\varepsilon_{k21}}{\varepsilon_{k32}} \tag{16}$$

Four kinds of convergence can occur.

- $0 < R < 1$ monolithic (MC)
- $-1 < R < 0$ oscillatory convergence (OC)
- $R > 1$ monotonic divergence (MD)
- $R < -1$ oscillatory divergence (OD)

The numerical error δ_k^* and order of accuracy P_k can be estimated by the generalized Richardson extrapolation method:

$$\delta_k^* = \frac{\varepsilon_{k21}}{r_k^{p_k} - 1} \tag{17}$$

$$p_k = \frac{\ln(\varepsilon_{k21}/\varepsilon_{k32})}{\ln(r_k)} \tag{18}$$

where, r_k is the refinement ratio between three solutions in grid and time step convergence studies. The GCI uncertainty U_k can then be estimated from numerical error δ_k^* multiplied by a factor of $F_s = 1.25$ to bound the numerical error:

$$U_k = F_s * \left| \delta_k^* \right| \tag{19}$$

In the present uncertainty study, three sets of mesh grids (i.e., fine, medium and coarse) and three sets of time step sizes were prepared to evaluate the numerical uncertainties caused by the mesh grid and time step. The wave-structure resonance condition ($\lambda/L = 1.2, H = 0.12$m, $U = 1.8$m/s) was selected as a representative case because large motions and loads tend to cause greater numerical errors (Tezdogan et al., 2015).

For mesh convergence study, the mesh region at free surface was refined progressively while with the mesh discretisation not altered in the background mesh. The medium time step size was selected of 0.0015s throughout all mesh convergence studies, and the total running time up to 15s with an approximate computational cost 72 CPU-hour. The detailed mesh refinement information were summarised in Table 5.

The time step convergence study was conducted with triple solutions using three lessened time step sizes ranging 0.001s, 0.0015s, 0.002s. The medium mesh condition G_2 was selected of representative case and the computational time consumed from the T_1 to T_3 were 96, 72 and 60 CPU-hours, respectively.

The uncertainty parameters of the amplitude values (heave, pitch and wave-induced VBMs) and the bow slamming pressure peaks (P_1 and P_2) for the mesh grids and time-step convergence were listed in Table 6 and Table 7, respectively. Moreover, the time-series of motion and pressure loads signals were plotted in Fig. 13 between physical time of 12s–15s. It is seen that reasonably small levels of uncertainty levels were achieved for the heave and pitch responses in both time-step and grid dependence tests. However, relatively large uncertainties U_G was estimated for the VBMs and slamming loads in mesh convergence study,

Table 5
Mesh grid information for convergence test.

Grid name	Hull form	Mesh	$\lambda/\Delta x$	$\lambda/\Delta z$	Gird number (million)
G_1	Intact	Fine	120	8	2.55
G_2		Medium	120	12	4.71
G_3		Coarse	120	16	6.83

Table 6
Convergence study for motions and loads by different grid schemes.

Parameter	Symbol	Amplitude value			Pressure peaks	
Description		Heave (m)	Pitch (°)	VBMs (Nm)	P_1 (pa)	P_2 (pa)
Fine solution	S_{G1}	0.0620	3.41	−234.6	2946.2	4306.0
Medium solution	S_{G2}	0.0615	3.36	−214.3	2916.1	4222.8
Coarse solution	S_{G3}	0.0608	3.28	−202.5	2907.2	4250.2
Refinement ratio	r_{G21}	1.45	1.45	1.45	1.45	1.45
Refinement ratio	r_{G32}	1.85	1.85	1.85	1.85	1.85
Convergence ratio	R_G	0.67	0.625	3.5	3.38	−3.04
Convergence type	–	MC	MC	MD	MD	OD
Order of accuracy	P_G	0.33	0.54	−0.76	5.97	–
Numerical error	δ_G^*	4.56	6.21	12.79	0.12	–
GCI uncertainty	U_G	5.97	8.27	18.33	0.16	–

Table 7
Convergence study for motions and loads by different time steps sizes.

Parameter	Symbol	Amplitude value			Pressure peaks	
Description		Heave (m)	Pitch (°)	VBMs (Nm)	P_1 (pa)	P_2 (pa)
Fine solution	S_{T1}	0.0619	3.39	−219.6	2969.8	4250.5
Medium solution	S_{T2}	0.0615	3.36	−214.3	2916.1	4222.0
Coarse solution	S_{T3}	0.0610	3.31	−195.5	2822.0	4206.0
Refinement ratio	r_{T21}	0.67	0.67	0.67	0.67	0.67
Refinement ratio	r_{T32}	0.75	0.75	0.75	0.75	0.75
Convergence ratio	R_T	0.57	0.60	0.30	0.56	1.75
Convergence type	–	MC	MC	MC	MC	MD
Order of accuracy	P_T	−2.44	−2.30	−4.29	−2.48	−0.32
Numerical error	δ_T^*	0.38	0.57	0.54	1.02	1.58
GCI uncertainty	U_T	0.48	0.72	0.68	1.29	5.99

mainly triggered by the numerical error from the coarse mesh. This implies that the wave and structure loads in the resonant case are very sensitive to the grid size resolution. Based on the considerations of the numerical accuracy and modelling effort, the medium mesh G_2 and medium time step T_2 were selected through all simulations in this study.

5. Results

In this section, the well-validated CFD-DMB method was further applied to understand the seakeeping and hydroelastic behaviours of the damaged ship with two damage scenarios, i.e., damaged tank numbers and tank positions. A series of time history results, including the volume of dynamic flooding water, global ship motions and structural loads of the damaged ships were presented. The virtual observations of the interactions among flooding water, seawater and the damaged ship were shown and analysed. The numerical results were then compared with the intact ship solutions and general suggestions for ship primary design and post-accident decisions were made.
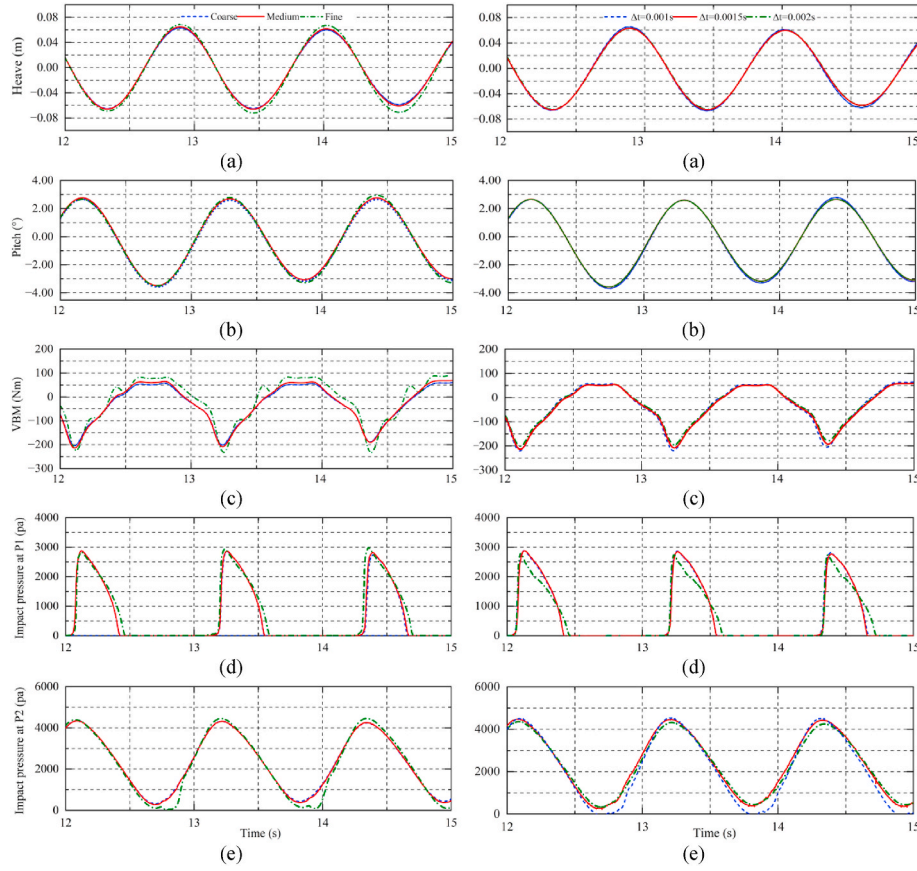
Fig. 13. Time series signals of the vertical motions, loads and slamming loads for the GCI uncertainty test.

5.1. The influence of the number of damaged tanks

In this section, a series of ship collision damage conditions (D1 to D3) were carried out for a systematic analysis of the damaged ship seakeeping and hydroelastic responses in head waves, as shown in Fig. 14. As mentioned in Section 3.2, the ship collision cases were investigated by having physical openings at ship's starboard and the three damaged positions were selected with the information given in Table 8. As mentioned before, all numerical investigations were performed in regular head waves with a wave height of $H = 0.12$m. The ship-wave resonance frequency ($\frac{\lambda}{L} = 1.2$) was adopted to obtain pronounced motion and load responses. A typical ship speed of Fn = 0.275 was selected to be consistent with that in the validation case.

5.1.1. Damaged tank and flexible ship motions

The time-series of the mass of the flooding water inside the damaged ship tanks were calculated for the prescribed three collision cases (D1 to D3), as shown in Fig. 15. It is seen that the dynamic flooding water

Table 8
Damage tank positions among damage conditions (D1, D2 and D3).

	Symbol	Full scale	Model scale
Damage opening compartment (S9) from FP	L_{S9} (m)	73	1.825
Damage opening compartment (S10) from FP	L_{S10} (m)	81.8	2.045
Damage opening compartment (S11) from FP	L_{S11} (m)	90.6	2.265

exhibits strong nonlinearity and a certain period. The mass of flooding water rises when severe sinkage occurs due to the increase in the ship draft. It is noticeable that the signal of the flooding water mass has subtle vibration areas (shaded in the figure). This phenomenon may occur by the interactions of the internal and the external sea water when damage openings emerge to the free surface due to the ship motions.

Physical views of the dynamic flooding water during green water events for three damaged ship cases in the resonant wave condition
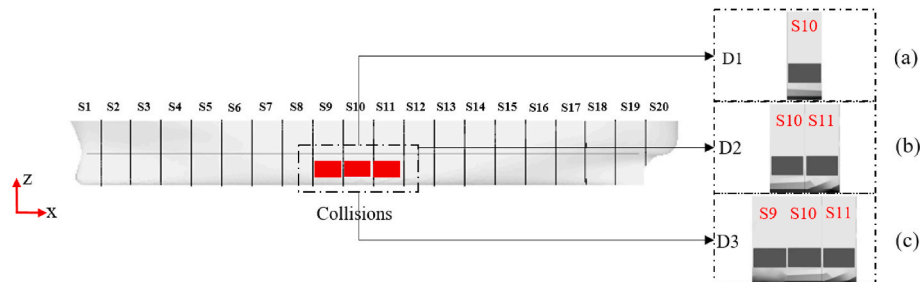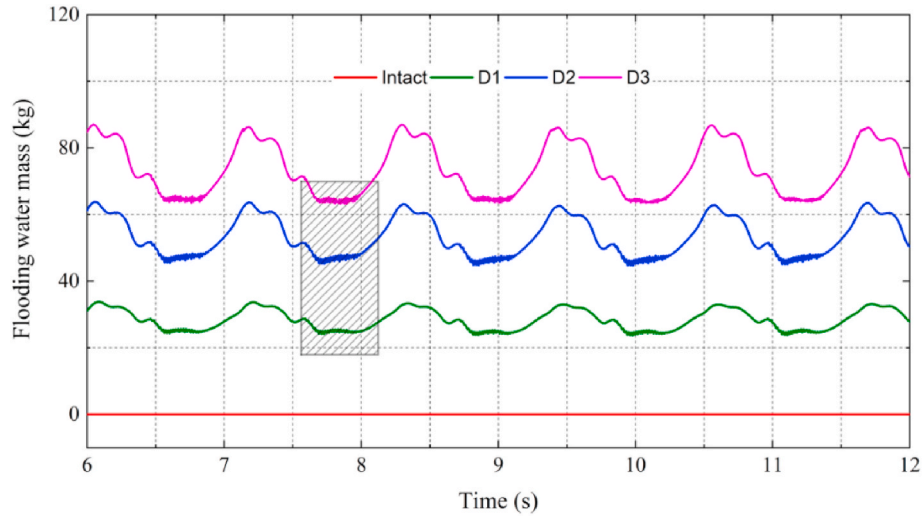

Fig. 14. Collision damaged ship layouts at front view with three damage opening conditions: (a) D1, (b) D2 and (c) D3.
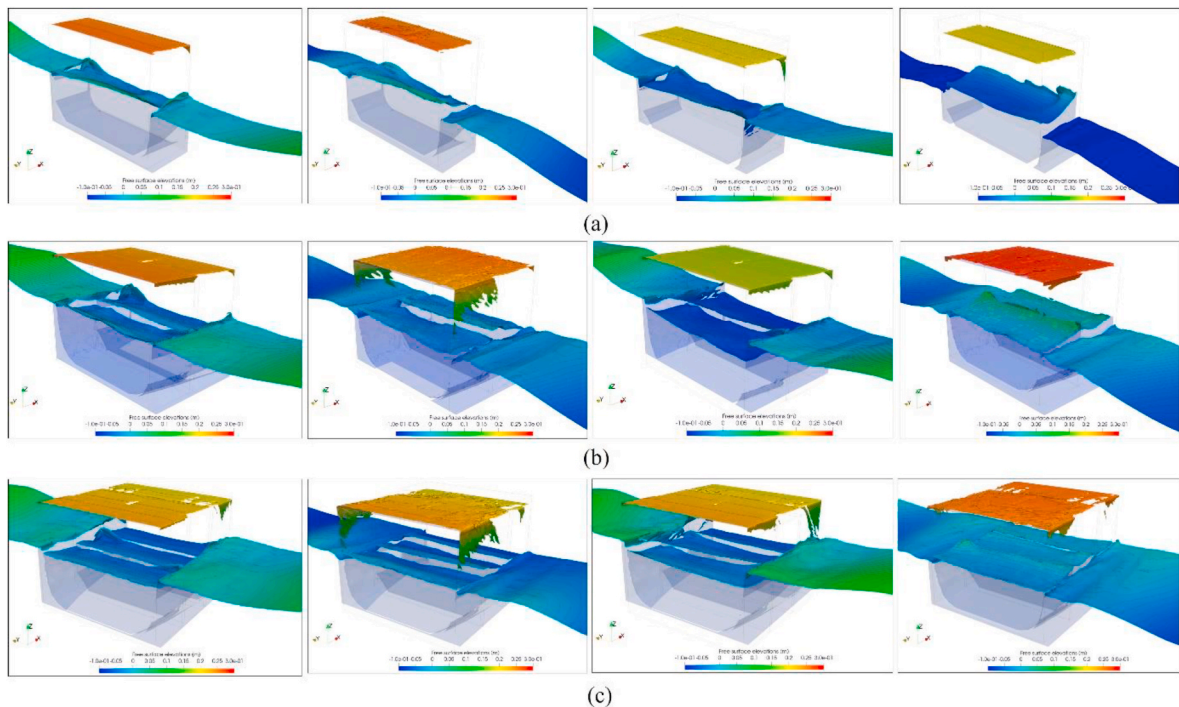
Fig. 15. Time series of dynamic flooding water mass volume in the case of ($\lambda/L = 1.2, H = 0.12$ m) of the intact ship with a comparison to three damaged conditions (D1 to D3).

($\lambda/L = 1.2, H = 0.12$ m) are shown in Fig. 16. The figure includes four snapshots inside a wave cycle, which shows the transient behaviour of the flooding water under the influence of ship motions. As it is seen that the dynamic flooding water sloshes (left and right) and heave/pitch (up and down) mildly inside the damage tanks. Meanwhile, the green water on deck phenomenon is violent through all cases, and the green water loads become another important issue which further affects the structural responses of the hull.

The vertical ship motions (heave and pitch) for the ship at intact and damaged conditions are studied in this section. The motion responses were measured on the beam node which is close to the ship's centre of gravity at a longitudinal position $x = 2.125$ m from the aft perpendicular, corresponding to 0.486 L. The original time-series of the heave and pitch motions of the ship in intact and three damaged conditions are shown in

Fig. 17. For heave and pitch signals, the positive sign represents the emergence of the ship and its trim by bow, respectively. It can be seen from the figure that the vertical motion signals of the intact and damaged ship at steady run region are in good accordance with standard sinusoidal signal in shape, which presents the same sinusoidal characteristics of the induced wave. The obvious ship sinkage can be found in the heave signals of the damaged ship conditions, due to the additional loads acting from the flooding water inside the damaged tank, i.e., hydrostatic and sloshing loads and thus changes the seakeeping behaviour of the ship.

The peak and trough values of the intact and damaged ship motions and their RAOs are summarised in Fig. 18 and Table 9, which show the effects of damaged tank numbers on the damaged ship vertical motions. As can be seen from the results, it can be concluded that the heave and
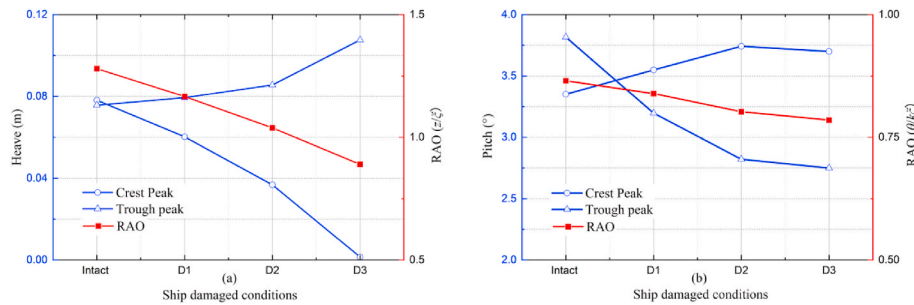

Fig. 16. Comparison of the dynamic flooding water inside the damaged tanks in the case of ($\lambda/L = 1.2, H = 0.12$ m) among three damaged conditions: (a) D1, (b) D2, (c) D3.
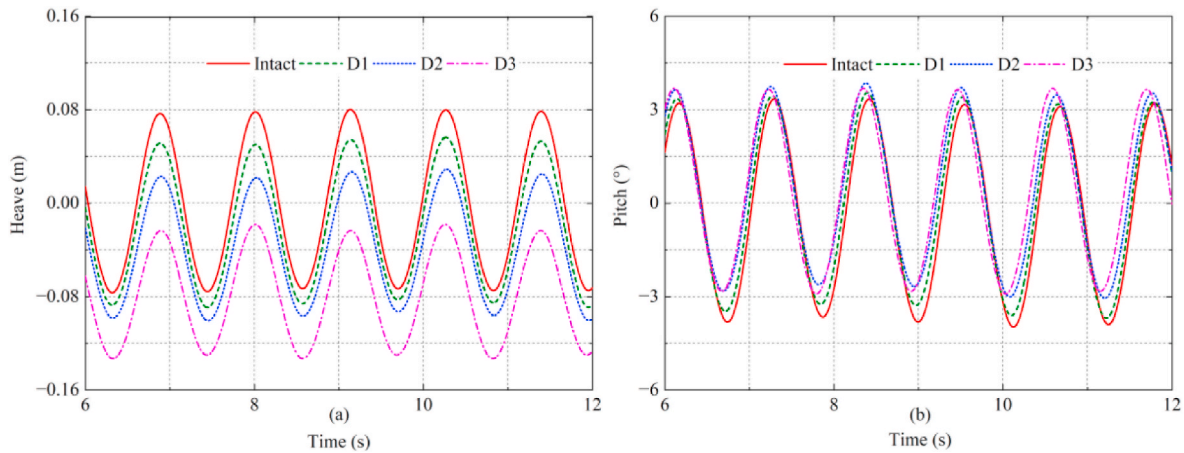
Fig. 17. Time series of the vertical ship motion responses in the case of ($\lambda/L = 1.2, H = 0.12$ m) of the intact ship compared to three damaged conditions (D1, D2 and D3): (a) heave motion, (b) pitch motion.

Fig. 18. Peak value distribution of ship motions in the case of intact ship and three damaged conditions (D1 to D3) (a) heave motions, (b) pitch motions.

Table 9
Numerical results of ship with intact and damaged ship conditions (D1, D2 and D3).

	Heave RAOs	Pitch RAOs	Peak Hogging moment (Nm)	Trough Sagging moment (Nm)	S_VBM (S10) (Nm)	Initial draft (m)
Intact	1.28	0.87	93.2	−233.6	256.5	−0.025
D1	1.16	0.84	115.4	−234.0	147.0	−0.035
D2	1.04	0.80	131.9	−228.6	40.5	−0.050
D3	0.89	0.78	145.0	−230.0	−19.59	−0.075

pitch responses reduced gradually from the intact ship condition to D3 with the growth of the intake water volume and the damage tank numbers. Similar results were also found by Folsø et al. (2008) and Lee et al. (2012) which supports our findings. In this case, the trough heave RAO value is much greater than the crest which indicates that the damaged ship was subjected to an obvious sinkage due to the added weight effects of the intake water inside the damaged tanks. For pitch motions, it can be seen that the intact ship initially experiences trim by bow motion and gradually shift towards to stern motion due to the changes of the longitudinal load distributions caused by the dynamic flooding water.
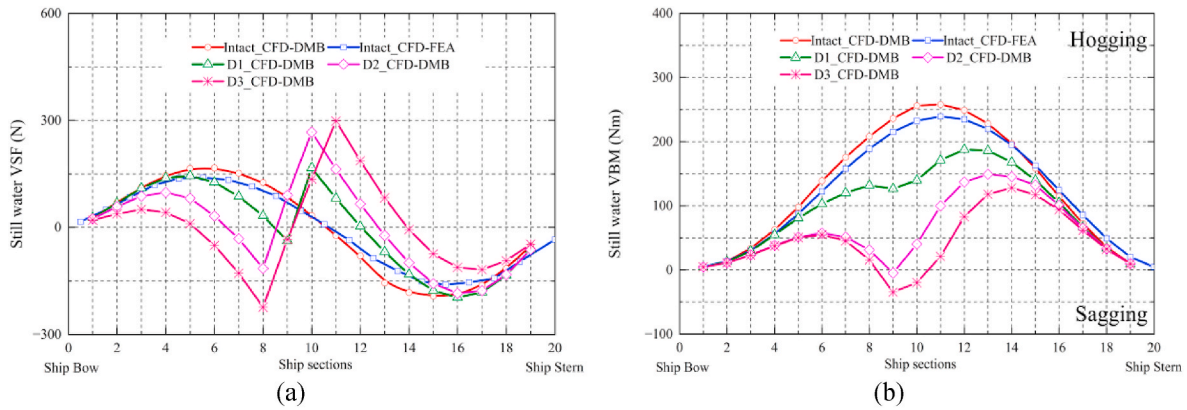
5.1.2. Still water VBMs of the ship

The calculated beam sectional loads for a damaged ship include the contributions of still water loads (S_VBM), wave-induced loads and flooding water loads. It is necessary to estimate the hull girder bending moments in still water primarily since it expresses the structural loads that a ship may experience during the vast majority of her service at sea. As aforementioned in Section 3.2, the sectional loads at each ship section

ranging from S1 to S19 were monitored for the intact and damaged ship in still water at a steady state and the peak values were extracted and shown in Fig. 19. The literature data (Jiao et al., 2021) for longitudinal distributions of still water VBM for the intact ship are also presented in the same figure for comparison and validation. The positive and negative of VBMs denote hogging and sagging loads, respectively. It can be seen that the S_VBM estimated by the present CFD-DMB method shows a similar trend with the results from the CFD-FEA method (Jiao et al., 2021), although the presented results slightly overestimate the hogging mangitudes of about 8.6% near the amidship sections. This deficiency may stem from the selections of different numerical methodologies and time steps. It can be seen from Fig. 19(b) that the intact ship stays in a perpetual hogging condition in still water and the maximum magnitude is achieved at Section 10 with a value of 256Nm. Similar findings were also obtained by Bouscasse et al. (2022)'s experimental study which found a 6750-TEU ship experiences perpetual hogging condition in still water. The magnitude of S_VBM reduced significantly at the damaged ship sections; the most obvious reduction can be found at the amidship section, i.e. Section 9.
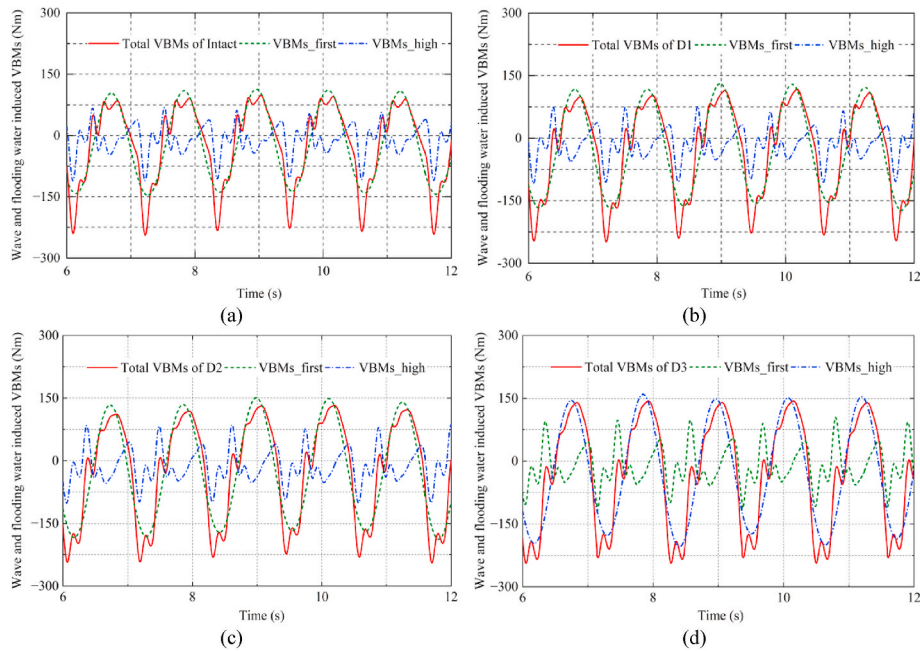
5.1.3. Wave and flooding water induced vertical bending moments

The wave and flooding water induced VBMs (W_VBMs) were calculated by subtracting the S_VBM from the total vertical bending moments (T_VBM). The time-series signals of both intact and three damaged ship conditions are summarised in Fig. 20. It can be seen that all W_VBMs show strong nonlinearity and asymmetric behaviours in which the sagging moments are dominant due to the vertical ship motions in waves.

An interesting finding is that as the number of damaged tanks and the volume of intake water increases, the trough of sagging moments basically does not change, however, a noticeable increase can be found in

Fig. 19. Hull girder loads of the ship at intact and damaged conditions with a comparison to the FSI simulations by Jiao et al. (2021a,b,c): (a) Still water vertical shear forces (S_VSF), (b) vertical bending moments (S_VBM).

Fig. 20. Wave and flooding induced vertical bending moments in the case of ($\lambda/L = 1.2, H = 0.12$ m) of the (a) intact ship, (b) D1, (c) D2, (d) D3.

the peak hogging moments. A bandwidth pass filter was applied to divide the W_VBMs data into two parts: the WF component (1st order harmonic wave loads) and HF components (includes high-order structure loads and nonlinear flooding water-induced loads). The time-series of the WF and HF components are plotted in Fig. 20 and their peak and trough values are summarised in Table 10. The results indicated pronounced HF components at the midship hull girder, and the magnitude of the HF components increased with the number of the damaged tanks from 57.2Nm (intact) to 91.4Nm (D3). The relevant frequency spectra of the W_VBMs of the ship at intact and damaged conditions were shown in Fig. 21. It is seen that the first-order harmonic wave encounter

Table 10
Peak and trough values of the first harmonic and high frequency of the W_VBMs.

Ship conditions	VBM_first harmonic (WF)(Nm)		VBM_high frequency (HF)(Nm)	
	Peak	Trough	Peak	Trough
Intact	112.1	−138.1	57.2	−105.5
D1	125.3	−165.3	67.5	−104.2
D2	142.2	−173.2	82.6	−98.6
D3	153.5	−185.2	91.4	−106.8

frequency and the springing frequency (up to 7th harmonic) showed good agreement between the target and calculated values. However, the peak value of the 2-node whipping frequency was generally lower than the values presented by coupled CFD-FEA models from (Jiao et al., 2021). This deficiency may be caused by three potential reasons: 1) Multibody formulation of three-node beam elements in MBDyn. The constraint equations were applied on beam elements as boundary conditions, which may introduce additional spurious eigenmodes related to the Lagrange multipliers. Usually, these eigenvalues related to those spurious modes may have a high damping value. 2) The implementation of structural damping in MBDyn. The damping effects on structural loads were studied by Lakshmynarayanana and Temarel (2020), which pointed out that the increase of structural damping from 0 to 0.01 may cause the reduction of the bending loads by about 25%. However, in the present study, it is necessary to apply structural damping to stabilize the structural solver and represent the material's actual damping behaviours. 3) Coupling algorithm inside the CFD-DMB framework. The implemented two-way loose coupling algorithm may cause deficiencies in capturing high-frequency components by comparison with a two-way strong coupling scheme. In general, the high-frequency components ($f > 8.0$ Hz) contributed less than about 5% of the total VBMs. The peak
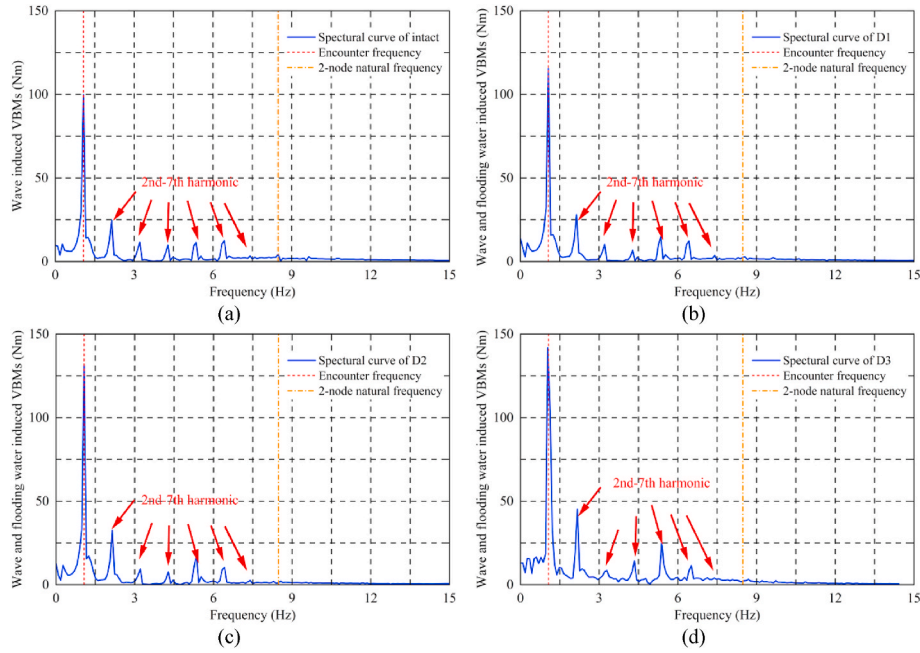
Fig. 21. The frequency spectra analysis of the wave and flooding induced VBMS in the case of ($\lambda/L = 1.2, H = 0.12$ m) of the (a) intact ship, (b) D1, (c) D2, (d) D3.

and trough values of the W_VBMs predicted by the present CFD-DMB method were shown generally acceptable agreements with both co-simulation results from Jiao et al. (2021) and experimental results from Chen et al. (2001). A systematic analysis of these potential issues will be presented as a future study.

Both WF and HF components of W_VBMs are non-dimensionalised by $M/\rho g L^2 B\xi$ and their peak values are plotted in Fig. 22. The numerical results show that the damaged tank numbers have less effects on the trough sagging moments, however, a growth of WF and HF hogging moments by about 26.9% and 31.5% can be noticed at three tanks damaged condition (D3) compared to that in intact ship. Similar results were also achieved by Begovic et al. (2013) and Begovic et al. (2017)'s experiments, in which a 28% of W_VBMs increase was reported for a damaged ship in head seas compared to the intact ship.

The predicted W_VBMs of the damaged ship at the cases of (D1-D3) were further compared to the new longitudinal strength standard for containerships URS11A issued by the International Association of Classification Societies (IACS,2005), as shown in Fig. 23. It can be seen that the URS11A regulation (Black solid line in figure) preserved large margin for the negative sagging moments due to the contributions of
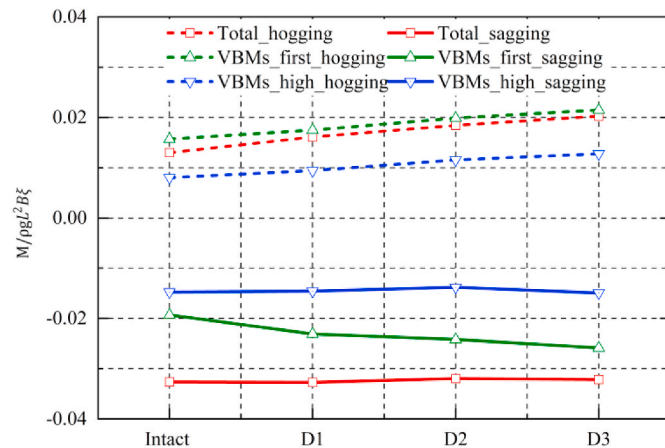
slamming-induced loads for ship in extreme waves, however, a very limited margin is reserved for the positive hogging moments. As can be found in Fig. 22, the predicted hogging moments at certain damaged ship sections exceed the limits proposed by the regulations, i.e., ship section 9 in the case of D2 and ship sections 8-10 in the case of D3. The excessive local W_VBMs may accelerate ship hogging deformation, which may result in the material buckling and further structural damages. This phenomenon may be one reason of MOL comfort accident, when buckling deformation occurs on the bottom shell plating, the intake water flushes inside the damaged tank and forces ship hogging until structural failure occurs. Although, a partial safety factor γ_{DB} for the hull girder hogging capacity was introduced in URS11A as 1.15, this factor may not be sufficient since the structure failure and buckling may occur while ship operates at ultimate strength. On the basis of the above results, this factor is recommended to be increased to be above 1.35 (shown in Fig. 23 with purple line) for damaged ship design in order to leave a safe margin of hogging moments to reduce the risk of secondary damages.
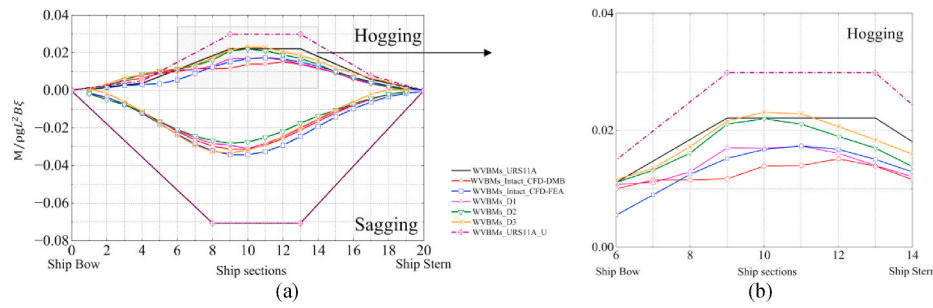
5.2. Analysis of the positions of the damaged tanks

The influences of the damaged tank positions on the damaged ship seakeeping and hydroelastic responses were carried out in this subsection utilising the present CFD-DMB method. Three different damaged tank positions were analysed and shown in Fig. 24, i.e., the damaged opening located at 5th, 10th and 15th stations from the bow in the cases of D4, D1 and D5, respectively. The detailed positions of each damage tank were summarised in Table 11. The same environment setting up as adopted in Section 5.1 was preserved in the CFD solver, in which the damaged ship operated in the ship-wave resonance frequency ($\frac{\lambda}{L} = 1.2, H = 0.12m, U = 1.8$m/s).

5.2.1. Flooding water mass and vertical ship motions

The estimation of the flooding water inside the damaged tank is significant, it mainly depends on the responses of the damaged ship; in return, the ship responses are also affected by the dynamic flooding water. The mass of the dynamic flooding water of the three damage conditions (D4, D1 and D5) were calculated and shown in Fig. 25. It is seen that the flooding water volume was greatly related to the damage

Fig. 22. Non-dimensional W_VBMs in the wave condition ($\lambda/L = 1.2, H = 0.12$ m) of the intact ship and the damaged conditions (D1 to D3).

Fig. 23. Longitudinal distributions of W_VBMs for the intact, damaged ship conditions (D1, D2 and D3) and URS11A regulation: (a) Normal version, (b) Zoomed version.
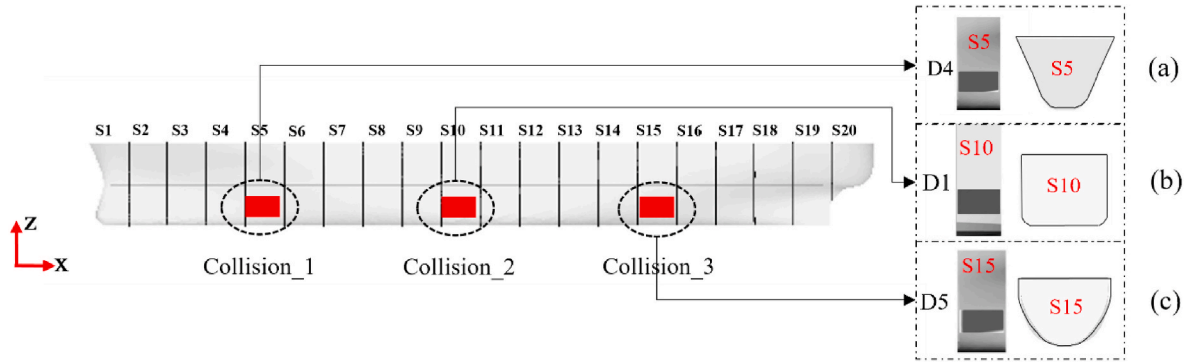
Fig. 24. Collision damaged ship layouts at front view with three damage opening conditions: (a) D4, (b) D1 and (c) D5.

Table 11
Damage tank positions among damage conditions (D4, D1 and D5).

	Symbol	Full scale	Model scale
Damage opening compartment (S5) from FP	L_{S5} (m)	35.8	0.895
Damage opening compartment (S10) from FP	L_{S10} (m)	81.8	2.045
Damage opening compartment (S15) from FP	L_{S15} (m)	127.76	3.194

locations. The maximum mass of flooding water was found in D1 due to the largest cross-section of the tank among the others. Meanwhile, the intake flooding water shows high nonlinearity for each damage condition; no certain period exhibited among these signals due to the complex interaction among the intake water, seawater and damaged ship.

Virtual observations of the flooding water profile inside the damaged tank are compared among three damaged conditions (D4, D1 and D5), as
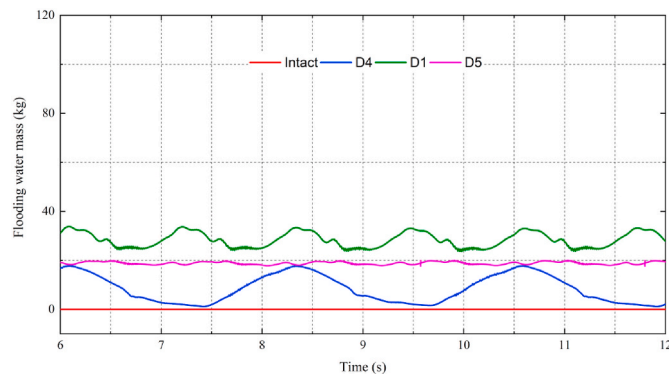
Fig. 25. Time-series signal of the mass of the dynamic flooding water of the intact and damaged ships.

shown in Fig. 26. It can be found that the damaged positions lead to different patterns of flooding water motions. In the case of D4, the water level rises and drops periodically in a sudden way due to the large amplitude of the pitch bow motions, while in D1 the water level changes much more smoothly. It is clear to see that the nonlinear sloshing effects are stronger in D5, in which the flooding water climbs up and impacts on the inner wall of the tank. For future studies, the region inside the damaged tank will apply a high-level mesh refinement to capture the local violent sloshing phenomenon.

To investigate the effects of damaged tank locations on ship motions in head waves, the peak, trough values of the heave and pitch responses and their RAOs at three damaged ship conditions were shown in Fig. 27 and compared to the results in the intact condition. It can be seen that the peak values of the heave and pitch motions are varied due to the fluctuations of the loading distributions among the three damaged conditions; accordingly, the KG and draft of the ship are modified so that the natural resonance periods of motions are shifted accordingly. It can be found that the damage opening at the amidship (D1) reduces both heave and pitch responses compared to the damages at ship section 5 (D4) and section 15 (D5). Meanwhile, the damaged tank position shifts the pitch from the bow motion (D4) to the stern motion (D5).

5.2.2. Vertical bending moments

The longitudinal distributions of the wave and flooding water-induced VBMs are non-dimensionalised at different ship sections for the intact ship and damaged conditions (D4, D1 and D5), as shown in Fig. 28. It can be seen that for the cases with only one damage tank, the peak and trough values of W_VBMs do not change significantly. However, the peak value of the hogging moments is found to shift along the ship longitudinal from ship section 9 (D4) to section 12 (D5). The peak hogging values of the intact and damage conditions are further compared with the URS11A regulation in Fig. 28(b), from which it can be concluded that the W_VBMs of the ship with a single damage tank regardless the damage tank position stay within the regulation limits.
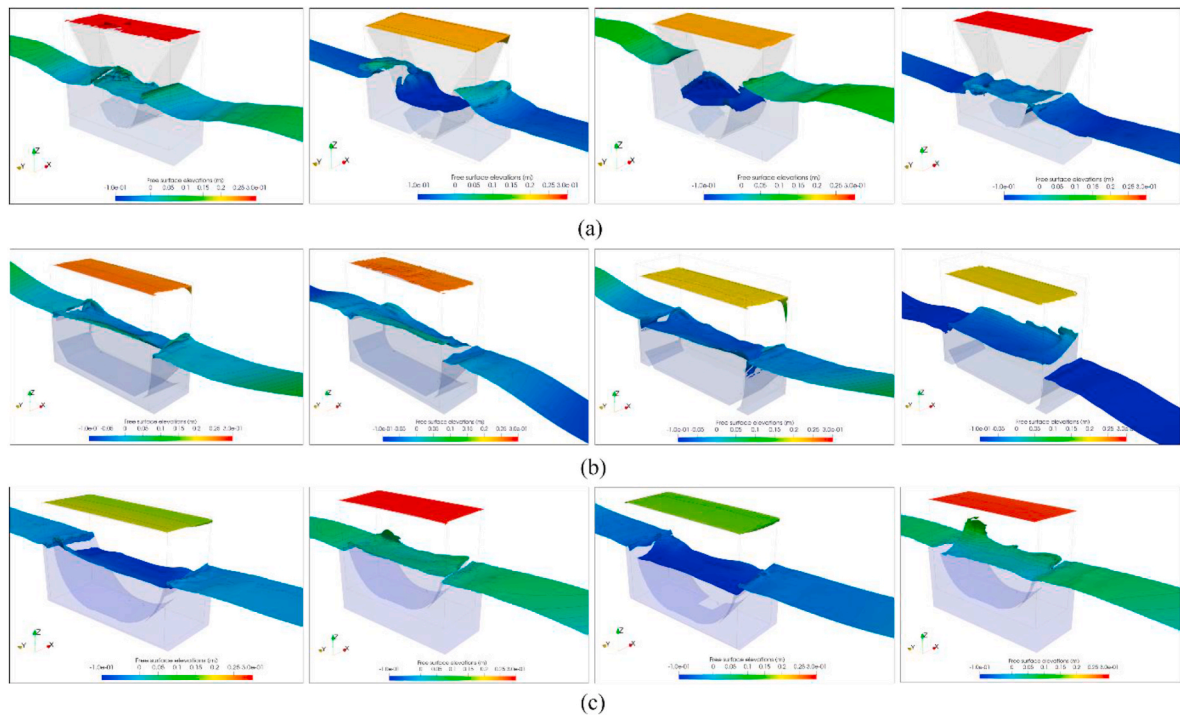
Fig. 26. Dynamic flooding water inside the damaged tanks comparison in the case of $(\lambda/L = 1.2, H = 0.12$ m$)$ among three damaged conditions: (a) D4, (b) D1, (c) D5.
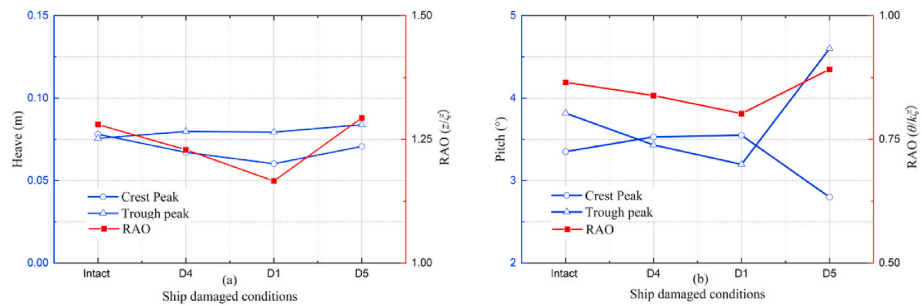

Fig. 27. Peak value distribution of ship motions in the case of intact ship and three damaged conditions (D4, D1 and D2) (a) heave motions, (b) pitch motions.
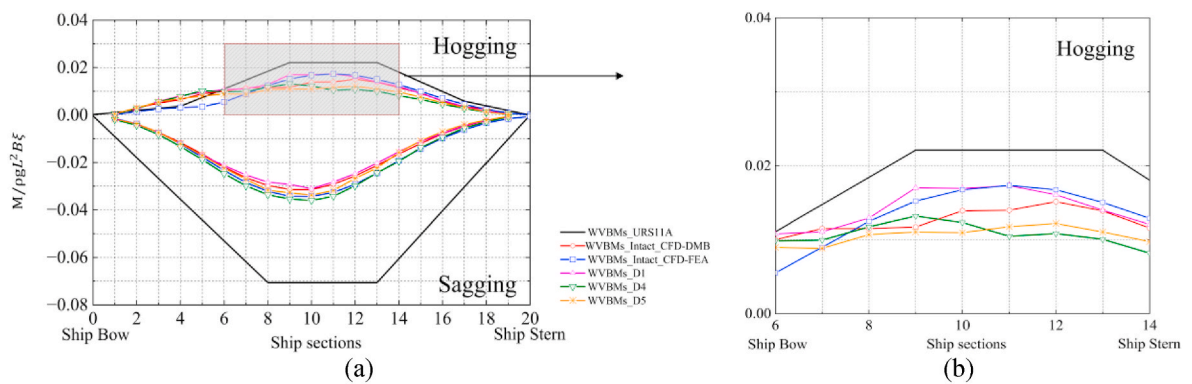

Fig. 28. Longitudinal distributions of W_VBMs for the intact, damaged ship conditions (D4, D1 and D5) and URS11A regulation: (a) Normal version, (b) Zoomed version.

6. Discussion and conclusion

This paper presents a two-way coupled FSI framework to investigate the hydroelasticity of a S175 containership model during intact and two

damaged scenarios in regular head waves as it travels at its operational speeds. The coupled CFD-DMB numerical tool was established, and in particular, OpenFOAM was chosen as the fluid solver, while the MBDyn was selected as the structure solver to solve the deformation of flexible

hull structure. A two-way implicit algorithm was implemented for robust coupling and to allow data communication between the fluid and structure solvers.

Two validation studies were presented first to evaluate the free surface capture capability of the multi-phase solver under severe sloshing conditions and wave-current generation conditions. The numerical results, including the measurements of the free surface elevations inside a 2D sloshing tank and the Stokes 2nd wave profile were shown in a good agreement with the experimental results and the theoretical values. Later, a GCI uncertainty test was carried out for the CFD solver on the seakeeping behaviour of a flexible intact ship in the wave-resonance ($\frac{\lambda}{L} = 1.2, H = 0.12$m) condition. The influences of the mesh grids and time step sizes which configured in CFD solver were evaluated by a series of numerical results based on the GCI uncertainty test, including the vertical ship motions (heave and pitch), structural loads at the midship section (VBMs) and slamming impact loads of the containership. The GCI analysis results show reasonably small uncertainty levels in time step sizes compared to the grid size resolution. As the computational grid in the CFD side becomes denser and the time step size decreases, the peak values and the high-frequency characteristics in the load responses become more apparent.

Afterwards, the seakeeping and hydroelastic analysis of the flexible ship with three damaged conditions (D1 to D3) in head waves were carried out using the present CFD-DMB method. The flooding water sloshing inside the damaged tanks and the exchange with the surrounding sea water was considered, detailed information, i.e., the time-varied volume flux and the virtual observations were drawn in Figs. 15 and 16, respectively. According to the numerical results, the heave and pitch motions at the case with three damaged tanks (D3) decrease by about 30.5% and 10.3% compared to the intact ship. Meanwhile, it is seen that clear sinkage and the shift of trim from bow to stern motion in time-series result (shown in Fig. 18) due to the variations of damaged loading conditions caused by the flooding water. The ultimate strength of the hull girder for a damaged hull was also calculated in this study by reducing the equivalent beam stiffness and applying strength reduction factors to account for loss of structural stiffness. The main finding is that the total VBMs at D3 is 30.3% larger than that of the intact ship. A similar result was also found by experiments of (Begovic et al., 2017) for a DTMB 5415 ship model which shows 28% increase in the total VBMs. In addition, the dynamic flooding water inside the damaged tanks was found to have a significant effect on the still water VBMs. The W_VBMs were calculated by subtracting the S_VBMs from T_VBMs. The results show that the peak hogging components of W_VBMs rises with the increase of mass of flooding water, however, the trough sagging moments experience less effects. The predicted W_VBMs were further compared to the new legislation of USR11A, which pointed out that the regulated hull girder hogging moments may be under-predicted at damaged ship conditions. The local W_VBMs at ship mid sections at the cases of D2 and D3 have been found to exceed the regulations limits by about 0.65% and 4.7%, respectively. In such circumstances, the structure may experience buckling and failure due to frequently operating in ultimate strength condition, which may result in secondary damage to the ship. Therefore, a safety factor of 1.35 is recommended in this paper based on the safety considerations which accounts for the increase of hogging moment induced by the dynamic flooding water.

The dynamic analysis was further carried out on the damaged scenarios with three damaged positions (D4, D1 and D5) to interpret the ship's elastic behaviours after collision damages. Virtual observations such as profile of flooding water surface, green water on deck and various hydrodynamic components were available in the numerical simulations. This information greatly facilitates analysis of the interactive dynamics of damaged ship, sea wave and flooding water. The ship hydroelasticity was studied based on the present FSI model with some important outputs. When damage opening located at amidship (D1), the ship responses of the heave and pitch became smaller, but the T_VBMs

was found to be the largest among the intact and other damage positions (D4 and D5). Meanwhile, the peak W_VBMs will shift along ship longitudinal direction based on the flooding tank position, i.e., ship section 9 at D1 and D4, ship section 12 at intact and D5. It can be further concluded that the damage of a single tank regardless its location will not cause the local VBMs exceeded than that in regulation (IACS, 2015), therefore, in such condition, the captain can prevent secondary accidents through the ascertainment of its cases and circumstance to make post-accident decision with less consideration of ship hydroelastic effects. Future work will present an experimental study on the flexible damaged ship with different damage scenarios in regular heading waves.

Recommendations for future research are briefly outlined below.

(1) Another important damage scenario, i.e., damage openings at the keel which may be caused by grounding, are recommended to investigate to prevent and minimise such accident causes. However, the residual strength of the ship is significantly affected due to the loss of the structure, and it should be accurately estimated by the loss of section modulus and the stiffness loss of the structure.

(2) The asymmetric structural loads, i.e., coupled horizontal bending moments and torsional moments induced by the flooding water, may lead to global ship roll motion and structural deformation, could be another research topic.

CRediT authorship contribution statement

Yujia Wei: Conceptualization, Methodology, Formal analysis, Writing – original draft. **Atilla Incecik:** Conceptualization, Writing – review & editing, Supervision. **Tahsin Tezdogan:** Conceptualization, Writing – review & editing, Supervision.

Declaration of competing interest

The authors declare that they have no known competing financial interests or personal relationships that could have appeared to influence the work reported in this paper.

Data availability

No data was used for the research described in the article.

Acknowledgements

References

Begovic, E., et al., 2017. An experimental study of hull girder loads on an intact and damaged naval ship. Ocean Eng. 133, 47–65.

Begovic, E., et al., 2013. Experimental assessment of intact and damaged ship motions in head, beam and quartering seas. Ocean Eng. 72, 209–226.

Bouscasse, B., et al., 2022. Experimental analysis of wave-induced vertical bending moment in steep regular waves. J. Fluid Struct. 111.

Ćatipović, I., et al., 2018. Seakeeping experiments on damaged ship. Ships Offshore Struct. 14 (Suppl. 1), 100–111.

Chan, H.S., et al., 2003. Global wave loads on intact and damaged Ro-Ro ships in regular oblique waves. Mar. Struct. 16 (4), 323–344.

Chen, R.Z., Du, S.X., Wu, Y.S., Lin, J.R., Hu, J.J., Yue, Y.L., 2001. Experiment on extreme wave loads of a flexible ship model. Practical Design of Ships and Other Floating Structures. In: Proceedings of the Eighth International Symposium on Practical Design of Ships and Other Floating StructuresPRADS (Practical Design in Shipbuilding) Chinese Academy of Engineering. Chinese Society of Naval Architects and Marine Engineers, Chinese Institute of Navigation.

Devolder, B., et al., 2018. Performance of a buoyancy-modified k-ω and k-ω SST turbulence model for simulating wave breaking under regular waves using OpenFOAM®. Coast. Eng. 138, 49–65.

Fols⊘, L., et al., 2008. Wave induced global loads for a damaged vessel. Ships Offshore Struct. 3 (4), 269–287.

Gao, Z.-l., Vassalos, D., 2015. The dynamics of the floodwater and the damaged ship in waves. J. Hydrodyn. 27 (5), 689–695.

Gao, Z., et al., 2013. Numerical study of damaged ship flooding in beam seas. Ocean Eng. 61, 77–87.

Gao, Z., Tian, X., 2021. Numerical study on the wave-induced roll motion of a damaged ship in head seas. Appl. Ocean Res. 114.

Ghiringhelli, G.L., Masarati, P., Mantegazza, P., 2000. Multibody implementation of finite volume C beams. AIAA J. 38 (1), 131–138.

Hashimoto, H., et al., 2017. A numerical simulation method for transient behavior of damaged ships associated with flooding. Ocean Eng. 143, 282–294.

Hirt, C.W., Nichols, B.D., 1981. Volume of fluid (VOF) method for the dynamics of free boundaries. J. Comput. Phys. 39 (1), 201–225.

Huang, S., Jiao, J., Soares, C.G., 2022. Uncertainty analyses on the CFD–FEA co-simulations of ship wave loads and whipping responses. Mar. Struct. 82.

IACS, 2015. Longitudinal strength standard for container ships. UR S11A, pp. 1–24. June 2015.

IMO, 2003. Interim guidelines for the approval of alternative methods of design and construction of oil tankers under Regulation 13F (5) of Annex 1 of MARPOL 73/78. Resolution MEPC 110 (49).

ITTC, 2017. ITTC Quality System Manual Recommended Procedures and Guidelines. Seakeeping Committe of the 28th ITTC.

Jacobsen, N.G., Fuhrman, D.R., Fredsøe, J., 2012. A wave generation toolbox for the open-source CFD library: OpenFoam. Int. J. Numer. Methods Fluid. 70 (9), 1073–1088.

Jasak, H., Jemcov, A., Tukovic, Z., 2007. OpenFOAM: a C++ library for complex physics simulations. Int. Workshop Coupl. Method. Num. Dyn. 1000, 1–20.

Jiao, J., et al., 2021a. A CFD–FEA two-way coupling method for predicting ship wave loads and hydroelastic responses. Appl. Ocean Res. 117, 102919.

Jiao, J., Huang, S., Soares, C.G., 2021b. Viscous fluid–flexible structure interaction analysis on ship springing and whipping responses in regular waves. J. Fluid Struct. 106, 103354.

Jiao, J., Huang, S., Tezdogan, T., Terziev, M., Soares, C.G., 2021c. Slamming and green water loads on ship sailing in regular waves predicted by coupled CFD–FEA approach. Ocean Eng., 110107

Lakshmynarayanana, P.A., Temarel, P., 2020. Application of a two-way partitioned method for predicting the wave-induced loads of a flexible containership. Appl. Ocean Res. 96, 102052.

Lee, Y., et al., 2012. Global wave loads on a damaged ship. Ships Offshore Struct. 7 (3), 237–268.

Liu, D., Lin, P., 2008. A numerical study of three-dimensional liquid sloshing in tanks. J. Comput. Phys. 227 (8), 3921–3939.

Lloyd's Register, 1996. World Casualty Statistics. Lloyd's Register of Shipping.

Manderbacka, T., et al., 2015. Transient response of a ship to an abrupt flooding accounting for the momentum flux. J. Fluid Struct. 57, 108–126.

Manderbacka, T., et al., 2019. An overview of the current research on stability of ships and ocean vehicles: the STAB2018 perspective. Ocean Eng. 186, 106090.

Masarati, P., Morandini, M., Mantegazza, P., 2014. An efficient formulation for general-purpose multibody/multiphysics analysis. J. Comput. Nonlinear Dynam. 9 (4), 041001.

Mikulić, A., et al., 2018. Wave-induced vertical motions and bending moments in damaged ships. J. Mar. Sci. Appl. 17 (3), 389–405.

Parunov, J., Ćorak, M., Gledić, I., 2015. Analysis and design of marine structures. In: Comparison of Two Practical Methods for Seakeeping Assessment of Damaged Ships, pp. 37–44.

Santos, T.A., Guedes Soares, C., 2008. Study of damaged ship motions taking into account floodwater dynamics. J. Mar. Sci. Technol. 13 (3), 291–307.

Siddiqui, M.A., et al., 2020. Experimental studies of a damaged ship section in beam sea waves. Appl. Ocean Res. 97.

Smith, C.S., 1977. Influence of local compressive failure on ultimate longitudinal strength of a ship's hull. Trans PRADS 1977, 73–79.

Soares, C., et al., 2009. Damage Assessment after Accidental Events: Report of Committee, vol. 1.

Stern, F., et al., 2006. Quantitative V&V of CFD simulations and certification of CFD codes. Int. J. Numer. Methods Fluid. 50 (11), 1335–1355.

Sun, Z., et al., 2021. Investigation of non-linear ship hydroelasticity by CFD-FEM coupling method. J. Mar. Sci. Eng. 9 (5).

Tezdogan, T., Demirel, Y.K., Kellett, P., Khorasanchi, M., Incecik, A., Turan, O., 2015. Full-scale unsteady RANS CFD simulations of ship behaviour and performance in head seas due to slow steaming. Ocean Eng. 97, 186–206.

Wei, Y., Tezdogan, T., 2022a. A fluid-strcuture interaction model on the hydroelastic analysis of a container SHIP using precice. In: 41st International Conference on Ocean, Offshore and Arctic Engineering **OMAE2022-78131**.

Wei, Y., et al., 2022. A fully coupled CFD-DMB approach on the ship hydroelasticity of a containership in extreme wave conditions. J. Mar. Sci. Eng. 10 (11), 1778.

Wei, Y., Tezdogan, T., 2022b. A fluid-structure interaction model on the hydroelastic analysis of a container ship using PRECICE. In: International Conference on Offshore Mechanics and Arctic Engineering. American Society of Mechanical Engineers.

Zhang, Y., et al., 2021. Study on the unequivalence between stiffness loss and strength loss of damaged hull girder. Ocean Eng. 229.